Journal of Heat Transfer

Technical Notes

This section contains shorter technical papers. These shorter papers will be subjected to the same review process as that for full papers.

Spectral Emittance of Particulate Ash-Like Deposits: Theoretical Predictions Compared to Experimental Measurement

S. P. Bhattacharya
e-mail: spb@cleanpower.com.au
Cooperative Research Centre for Clean Power from Lignite, 8/677 Springvale Road, Mulgrave, Victoria 3170, Australia

This note presents results of a theoretical and experimental investigation on the emittance of particulate deposits. A simple model based on independent and multiple scattering and using discrete ordinate method has been developed to predict the spectral hemispherical and normal emittance of particulate deposits. The model predictions are compared with measurements carried out under this study-controlled spectral emission measurements between wavelengths of 2 and 12 μm on deposits of ground synthetic ash particles having known composition and particle size. The trends from the predictions matched well with the measured values, except for some differences in the wavelength region below 4 μm, and between 8 μm and 12 μm wavelength. Possible reasons for these differences are discussed. [DOI: 10.1115/1.1666885]

Keywords: Absorption, Experimental, Heat Transfer, Radiation

Introduction

Determination of emittance of particulate deposits is important in several applications such as radiative heat transfer and on-line monitoring of deposits in pulverised fuel (*pf*) fired furnaces [1], state of refractory in industrial furnaces [2], remote sensing, high-temperature energy saving materials, and stealth technology. Emittance (ε) of a surface, particulate or otherwise, is commonly defined as the ratio of its emission rate (E) to that from a blackbody (E_B) at the same temperature ($\varepsilon = E/E_B$). Emittance can be defined as hemispherical (ε_h) or normal (ε_n) depending on the direction of measurement, and as spectral (ε_λ) or total (ε_t) in which case it is referred to part or the entire wavelength spectrum with reference to the direction and spectral range. It can be defined as a combination of any two of the above. Spectral emittance can be used to calculate the total emittance [3]. Studies on emittance of particulate deposits are not common, particularly both modeling and spectral measurements with particle size relevant to deposits in *pf* fired furnaces. Studies by Boow and Goard [4] and Brajuskovic et al. [5] are on total emittance measurements of deposits at surface temperatures ranging from 200 to 1000°C showing the effect of temperature on total emittance. The study by Wall and Becker [3] is on spectral band measurements at temperatures ranging from 700 to 1000°C and shows the effect of iron content and temperature. The study by Markham et al. [6] is the only study, which shows comparison of theoretical and measured values of spectral emittance of ash deposits. Their model was based on 2-flux theory, and the model used an adjustable value for the asymmetry parameter (g) to get good match with measured values. Studies by Wall et al. [7] and Bhattacharya et al. [8,9] present theoretical predictions and separate measurements on the effects of particle size and concentration, physical state, heating, and iron content on spectral emittance of ash deposits. However, the predictions were not directly compared with measurements of the same particle size.

This paper presents results from a theoretical and experimental study on emittance of ash-like particulate deposits. A simple model has been developed for prediction of spectral hemispherical and spectral normal emittance of particulate deposits. The predictions can be made as a function of particle size, particle concentration, and optical constants (real and absorption indices, which in turn are function of chemical composition). Predictions from the model are then compared with spectral measurements on ash-like particulate deposits using emission spectrometry.

Model and Input Parameters

The ash deposit is modeled to be one dimensional axisymmetric layer. The equation for radiative transfer [10] is approximated using the discrete ordinate method with 16 ordinate directions, and weighting fractions corresponding to the solid angle represented [11]. Using appropriate boundary conditions, spectral reflectance (ρ) and spectral transmittance (τ) of the layer is calculated, from which absorbance (α) can be calculated as follows:

$$\alpha = 1 - \tau - \rho \tag{1}$$

According to Kirchoff's law, spectral emittance is equal to the spectral absorbance which may be evaluated from Eq. (1). For an opaque deposit, the thickness of the layer can be adjusted so that spectral transmittance is 2 percent or less, which is arbitrarily assumed to be the limit of opacity in the calculations. Spectral single particle properties (scatter matrix, extinction efficiency) were calculated using Mie theory using a code in Bohren and Huffman [12]. The following assumptions are made in the model: the particles in the deposit are spherical in shape, and all particles have same chemical composition, i.e., they have same complex refractive index. Also, only independent and multiple scattering is considered in the model. Further details of the model are available in Bhattacharya [13].

The model requires complex refractive index—real (n) and absorption index (k), density of deposit materials, and particle size (or distribution) as input parameters. Values of these input parameters were taken from Goodwin [14]. The samples used for model

Contributed by the Heat Transfer Division for publication in the JOURNAL OF HEAT TRANSFER. Manuscript received by the Heat Transfer Division September 11, 2002; revision received July 1, 2003. Associate Editor: S. T. Thynell.

Table 1 Composition (wt%) and Density (kg/m^3) of the samples

Sample	SiO_2	Al_2O_3	CaO	Fe_2O_3	Density
S2	54.95	27.25	15.80	2.00	2550
S10	50.46	24.87	14.67	10.00	2630

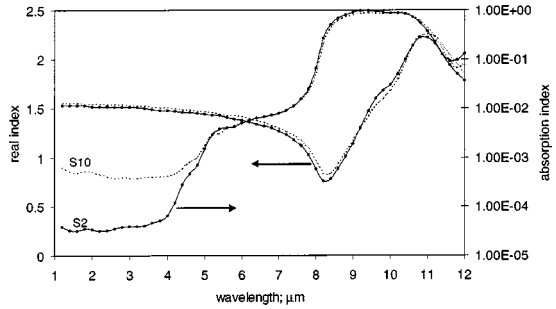

Fig. 1 Spectral complex refractive index of the samples used in model predictions [14]

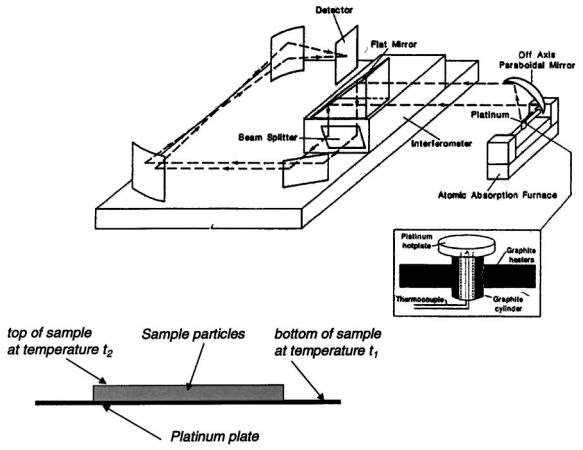

Fig. 2 Experimental setup (published with permission from Applied Spectroscopy)

predictions and in experiments vary in iron content from 2 percent to 10 percent. Goodwin obtained the real and absorption indices, *n* and *k*, from normal reflectance and transmission measurements on polished wafers of synthetic ash slags. Table 1 shows the composition and density, and Fig. 1 shows the spectral complex refractive index of the samples. As is evident from Fig. 1, the spectral absorption index increases with increasing iron content between wavelengths from 1.2 to 4 μm; thereafter the values are similar. The real index shows little increase with iron content between 1.2 and 8 μm wavelength. It varies from about 1.6 at 1.2 μm wavelength to below 1 at 8 μm, thereafter rising above 2. Among the samples, sample S2 is weakly absorbing and sample S10 is strongly absorbing. The predictions made in this paper are for isothermal and opaque deposits consisting of monosized particles, and for spectral normal measurements. A modified form of the model can also be used for prediction of spectral hemispherical emittance, apparent emittance of nonisothermal particulate deposits opaque and semi-transparent deposits [9], and radiative heat transfer calculations in one-dimensional geometry.

Experimental Work

Experimental work involving emission spectrometry was undertaken on particulate deposits to measure their spectral normal emittance, which are then compared with model predictions. The experimental equipment is located at the Division of Coal and Energy Technology, CSIRO at North Ryde in Sydney. It has primarily been used to study the structural changes occurring in coal and other minerals on heating [15,16]. The infrared emission cell consists of a modified atomic absorption graphite rod furnace and is illustrated in Fig. 2. The furnace was driven by a thyristor controlled ac power supply capable of delivering up to 150 amps at 12 volts. A platinum disk (6 mm diameter), which acts as a hotplate to heat the sample, is placed on the graphite rod. An insulated 125 μm type *R* thermocouple was embedded inside the platinum in such a way that the thermocouple junction was <0.3 mm below the surface of the platinum (Fig. 2 inset). Temperature control of ± 3°C at the maximum operating temperature of 1500°C was achieved by using an Eurotherm Model 808 proportional temperature controller, coupled to the thermocouple. An off-axis paraboloidal mirror with a focal length of 25 mm mounted above the heater captured the infrared radiation and directed it into a Digilab FTS-60A Fourier transform infrared spectrometer. The heater assembly was located so that the surface of the platinum was slightly above the focal point of the off-axis paraboloidal mirror. With this geometry, a spot of approximately 3 mm diameter is sampled by the spectrometer. The modifications to the spectrometer involved the removal of the aperture assembly and replacing it with a mirror. Reflection of modulated radiation back from the interferometer to the sample with subsequent additional modulation has been identified as a problem with this type of measurement. Very little distortion of the spectra due to this effect is observed. A room temperature Deuterated Triglycine Sulfate (DTGS) detector was used and as a result is not responsive to emission from surrounding objects. The entire spectrometer and sample furnace was covered with a perspex box which was purged with nitrogen to remove IR absorption by water vapor and carbon dioxide in the path of the sample emission.

Samples Used. Two different particulate samples were used in the measurement. These are slag samples ground after melting oxide mixtures at 1550°C in proportion similar to those found in power station ash. Particles of such samples are expected to be of uniform composition, which is presented in Table 1. To illustrate the effect of size on emittance, sample S2 (2 percent Fe_2O_3) was separated into two size groups, one having a size range of 5–35 μm (Sauter mean diameter of 12.9 μm), the other being sieve sized 45–53 μm. One size group of the sample S10 was used in the experiment, with a size range of 5–33 μm (Sauter mean diameter of 14.9 μm). A comparison of emittance between the samples S2 and S10 is intended to illustrate the effect of composition.

Experiment Procedure. The sample to be analyzed is carefully spread over the platinum surface. The sample heated to the desired temperature, was held at this temperature while accumulation of single beam spectrum took place. The spectra were recorded with the use of 64 scans at a nominal resolution of 4 cm^{-1}. The emittance measured at 600°C is used in this paper. A graphite plate with the same geometry as that of the platinum plate was used to approximate a blackbody source. Spectra from the graphite plate and the platinum plate were acquired at the same temperatures as those of the samples and stored for later use.

To ascertain the opaqueness, the samples were first subjected to transmission measurements before undertaking emission experiments. Thus for the same sample, two sets of spectral measurements, transmission and emission, were carried out. An infrared microscope was used for the purpose and the sample particles were spread horizontally over a 6 mm diameter area of a KBr window. For all the samples, concentration was such that the spectral transmittance across the layers was between 1 and 10 percent, but mostly under 2 percent. This amounted to using approximately

10 mg of sample. This compared favourably with the findings from another study [8] by the author, where it was observed that a sample density of about 400 gm/m^2 resulted in an opaque layer ($<$2 percent transmittance) for such samples.

Calculation Procedure. For a sample particulate layer distributed on the platinum plate during measurement (as shown in Fig. 2) emittance was determined as follows:

$$\varepsilon_{S,\lambda} = \left(\frac{I_{S,t2} - \tau \times I_{bg,t1}}{I_{bb,t2}} \right) \times \varepsilon_{g,\lambda} \quad (2)$$

where,

I_S = the intensity from the sample, as measured
I_{bg} = the intensity from the platinum plate, as measured
I_{bb} = the intensity from the graphite plate, as measured
τ = transmission across the sample, average of three measurements from the IR microscope
ε_g = spectral emittance of graphite, from Toloukian and Ho [17]

The temperature t_1 is measured during the experiment, whereas t_2 depends on the thermal conductivity (k) and thickness (t) of the sample layer, and radiative (and/or convective) loss from the surface. The transmittance (τ) depends primarily on the layer thickness. A procedure to estimate the top temperature t_2 and its effect on sample emittance is outlined in Bhattacharya [13]. It was observed that for the sample mass used in the experiment, the temperature t_2 was not significantly below the temperature t_1, and therefore, $I_{bb,t1}$ (which was measured) instead of $I_{bb,t2}$ was used in Eq. (2) to estimate the sample emittance. The contribution from the intensity emitted from the platinum plate was taken into account using Eq. (2). Data manipulation was performed on the interferograms.

Estimation of Error. The error estimation procedure has been formulated following Coleman and Steele [18]. The sources of error involve uncertainties in transmission measurement, uncertainties in the spectral emittance of the graphite plate, uncertainties in measurement of the intensity from the graphite plate, platinum plate and the samples. The details are presented in Bhattacharya [13]. The overall error in the measured emittance is estimated to be ± 0.06.

Comparison of Predicted and Measured Emittance

Effect of Size. Results of model predictions and measurements are presented in Figs. 3 and 4. In Fig. 3, predictions are made for the upper, lower and the mean size of the particles used. In Fig. 4, predictions are shown only for the mean size of the sample. In both figures, particulate character, as predicted earlier,

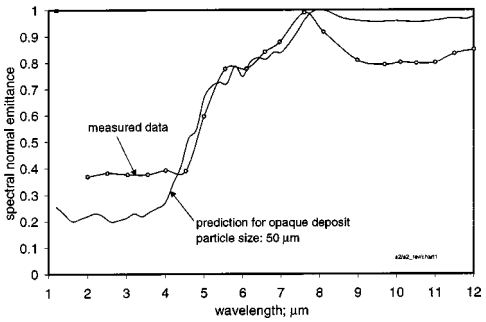

Fig. 4 Comparison of measured and predicted emittance of ash-like particulate deposits: sample S2, size range; 45–53 μm, mean diameter 50 μm.

of the emissive layer is evident. Measured emittance, as well as the predicted values are close to 1 between 7 and 8 μm wavelength. This is the region of Christiansen Effect, where real index (n) of the sample is 1, the real index of the surrounding medium. In fact, Goodwin's samples have real index of 1 between 7 and 8 μm wavelength. Apart from the reason of having similar composition, the similarity in real index values justifies the use of the complex refractive index of Goodwin's samples in the predictive calculations.

The model appears to underpredict emittance at wavelength below 4 μm, and overpredict above 8 μm wavelength. The model considers independent theory, multiple scattering, homogeneous composition and spherical particles. The slag particles are expected to be of homogeneous composition because of melting during preparation. Also, the radiative properties of an aggregate of irregular shaped particles are not affected significantly by the deviation of their shape from spherical [19,20]. Therefore, a comparison of the figures shows largely the effect of size on emittance, rather than the effects of irregular shape or inhomogeneous composition. Also, the larger particles recorded higher emittance, a trend consistent with predictions. The measurements indicate that spectral emittance of particulate deposits could be as low as 0.3 at low wavelengths, supporting the trend in model predictions and industrial measurements reported by Carter et al. [21]. The effect of particle size is primarily limited to the wavelength region below 6 μm, again supporting the predictions.

Apart from composition and particle size, emittance of a deposit depends on strongly coupled ways with its thermal conductivity, porosity and physical structure [22]. The effects of Dependent interactions, physical structure, or possible variation in thermal conductivity of the particles have not been considered in the simple model. Even then, good qualitative agreement is evident between the predicted and measured values.

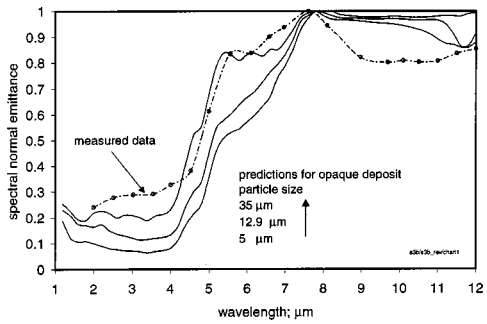

Fig. 3 Comparison of measured and predicted emittance of ash-like particulate deposits: sample S2, size range; 5–35 μm and sauter mean diameter 12.9 μm.

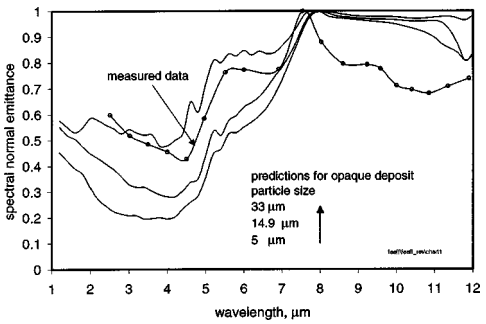

Fig. 5 Comparison of measured and predicted emittance of ash-like particulate deposits: sample S10, size range; 5–33 μm and sauter mean diameter 14.9 μm.

In a *pf* fired furnace, low wall emittance such as 0.3 may result in a decrease in heat absorption, and, therefore, in an increase in furnace exit temperature. The approximate changes in furnace exit temperature may be estimated by a well-mixed furnace model [23]. The model assumes a uniform build-up of ash deposits over the complete furnace walls, and requires, among others, total absorbance of the wall deposits as input. Spectral absorbance of a deposit is equal to the spectral emittance and the total absorbance of a deposit may be estimated once the spectral emittance and the flame temperatures are known [7]. It is estimated that for a 660 MWe *pf* fired furnace, a change in wall emittance from 0.7 (clean tube) to a low value of 0.3 affects the furnace heat absorption in a way that the exit gas temperature increases by 150°C.

Effect of Composition. Figure 5 shows the measured emittance of particulate deposits of sample S10. The ground particles of samples S2 and S10 had Sauter mean diameters of 12.9 μm and 14.9 μm, respectively. Both these samples had comparable amounts of silica, alumina and calcium oxide, and also similar particle sizes, so that a comparison of Figs. 3 and 5 reveals the difference predominantly due to the variation in iron content. As is evident, sample S10 with the higher iron content gave a higher emittance and the effect of iron is limited to wavelengths below 5 μm, a trend matched with the predictions [9]. The increase in emittance with iron content is due to the higher absorption index associated with high iron bearing sample (Fig. 1) at low wavelengths. As may be seen from Fig. 5, sample S10 showed a sharp drop in emittance at all temperatures going from 2 to 4 μm wavelength. In a separate experimental study involving reflectance and transmission spectroscopy (as opposed to emission and transmission spectroscopy used in this study), Bhattacharya et al. [8] observed that the difference between independent theory based predictions and the measured emittance of an opaque deposit is greater for weakly absorbing samples than strongly absorbing samples. Similar observations can be noted from Figs. 3–5.

Conclusions

This note presents results of a theoretical and experimental investigation of the emittance of particulate deposits. A simple model based on independent and multiple scattering has been developed to predict the spectral emittance of particulate deposits. The model predictions are compared with spectral emission measurements between 2 and 12 μm wavelength on deposits of ground synthetic ash particles having known composition and particle size. Emittance of particulate deposits is highly spectral. The measurements and the predictions show that fine particulate layers could be reflective, with emittances less than 0.3 especially at wavelengths below 4 μm. Such layers are formed during the initiation of deposits in *pf* furnaces. Layers of coarse particles are predicted to have higher emittance, a trend matched by measurements under this study. The effect of composition, in particular iron content, on emittance of deposits is found to be significant, with samples having higher iron content recording higher emittance. The effects are limited primarily to the wavelength region below 6 μm. This region is of primary interest to radiative heat transfer in *pf* fired furnaces. Even though there is good qualitative agreement between the model predictions and measured values, there are differences in the 1–4 μm wavelength, and again between 8–12 μm wavelength region. Further modeling efforts should be expended in improving the predictions, particularly incorporating the dependent effects [8]. Very few studies have been reported in the literature dependent effects have on emittance of ash deposits. All these studies [24–26] are limited to either very small particles (Rayleigh size) or very large particles (geometric range), but none of intermediate size range relevant to ash deposits in *pf* fired furnaces.

Acknowledgment

The author acknowledges Dr. Tony Vassallo of the CSIRO, Division of Energy Technology for allowing the use of his equipment, and assistance during measurements.

References

[1] Elliston, D. G., Gray, W. A., Hibberd, D. F., Ho, T. Y., and Williams, A., 1987, "The Effect of Surface Emissivity on Furnace Performance," J. Inst. Energy, pp. 155–167.
[2] Debellis, C. L., 1991, "Effect of Refractory Emittance in Industrial Furnaces," *Fundamentals of Radiative Heat Transfer*, HTD Vol. 160., pp. 104–115.
[3] Wall, T. F., and Becker, H., 1984, "Total Absorptivities and Emissivities of Particulate Coal Ash from Spectral Band Emissivity Measurements," ASME J. Eng. Gas Turbines Power, **106**, pp. 771–776.
[4] Boow, J., and Goard, P. R. C., 1969, "Fireside Deposits and Their Effect on Heat Transfer in a Pulverised Fuel Fired Boiler," Fuel, pp. 412–418.
[5] Brajuskovic, B., Uchiyama, M., and Makino, T., 1991, "Experimental Investigation of Total Emittance of Power Plant Boiler Ash Deposits," Experimental Heat Transfer, Fluid Mechanics, and Thermodynamics, J. F. Keffer et al., eds., Elsevier.
[6] Markham, J. R., Solomon, P. R., Best, P. E., and Yu, Z. Z., 1992, "Measurement of Radiative Properties of Ash and Slag by FT-IR Emission and Reflection Spectroscopy," ASME J. of Heat Transfer , **114**, pp. 458–464.
[7] Wall, T. F., Bhattacharya, S. P., Zhang, D. K., Gupta, R. P., and He, X., 1993, "The Properties and Thermal Effects of Ash Deposits in Coal Fired Furnaces," Prog. Energy Combust. Sci., **19**, pp. 487–504.
[8] Bhattacharya, S. P., Wall, T. F., and Schuster, M. A., 1997, "A Study on the Importance of Dependent Radiative Effects in Determining the Spectral and Total Emittance of Particulate Ash Deposits in Pulverised Fuel Fired Furnaces," J. of Chemical Engineering and Processing, **36**(6), pp. 423–432.
[9] Bhattacharya, S. P., 2000, "A Theoretical Investigation of the Influence of Optical Constants and Particle Size on the Radiative Properties and Heat Transfer Involving Ash Clouds and Deposits," J. of Chemical Engineering and Processing, **39**(5), pp. 471–483.
[10] Siegel, R., and Howell, J. R., 1992, *Thermal Radiation Heat Transfer*, Hemisphere Publishing, Washington.
[11] Chandrasekhar, S., 1960, *Radiative Transfer*, Dover Publications, NY.
[12] Bohren, C. F., and Huffman, D. R., 1983, *Absorption and Scattering of Light by Small Particles*, John Wiley and Sons.
[13] Bhattacharya, S. P., 1995, "The Radiative Properties and Thermal Effects of Ash Clouds and Deposits in Pulverised Fuel Fired Furnaces," Ph.D. Thesis, The University of Newcastle, Australia.
[14] Goodwin, D. G., 1986, "Infrared Optical Constants of Coal Slags," Ph.D. thesis, Stanford University.
[15] Vassallo, A. M., Cole-Clarke, P. A., Pang, L. S. K., and Palmisano, A. J., 1992, "Infrared Emission Spectroscopy of Coal Minerals and Their Thermal Transformations," Appl. Spectrosc., **46**(1), pp. 73–78.
[16] Vassallo, A. M., and Finnie, K. S., 1992, "Infrared Emission Spectroscopy of Some Sulfate Minerals," Appl. Spectrosc., **46**(10), pp. 1477–1482.
[17] Touloukian, Y. S., and Ho, C. J., 1989, Thermal Radiative Properties of Nonmetallic Solids, **8**, Plenum Press, New York.
[18] Coleman, W., and Steele, G., 1989, *Experimentation and Uncertainty Analysis for Engineers*, John Wiley, NY
[19] Viskanta, R., and Menguc, M., 1987, "Radiation Heat Transfer in Combustion Systems," Prog. Energy Combust. Sci., pp. 97–160.
[20] Wenlan, X., and Shen, S. C., 1997, "Infrared Emittance of Medium Containing Nonsphere-Shaped Particles," Applied Optics, **36**(7), pp. 1644–1649.
[21] Carter, H. R., Kokdsal, C. G., and Garabrant, M. A., 1992, "Furnace Cleaning in Utility Boilers Burning Powder River Basin Coals," *Proc. International Power Generation Conference*, Atlanta.
[22] Baxter, L. L., 1993, "In Situ Real Time Emission FTIR Spectroscopy as a Diagnostic for Ash Deposition During Coal Combustion," *Proc. Engineering Foundation Conference*, Solihull, UK.
[23] Hottel, H. C., and Sarofim, A. F., 1967, *Radiative Transfer*, McGraw Hill.
[24] Yamada, Y., Cartigny, J. D., and Tien, C. L., 1986, "Radiative Transfer With Dependent Scattering by Particles: Part 2—Experimental Investigation," J. Heat Transfer, **108**, pp. 608–613.
[25] Kumar, S., and Tien, C. L., 1990, "Dependent Absorption and Extinction of Radiation by Small Particles," J. Heat Transfer., **112**, pp. 178–185.
[26] Mazza, G. D., Berto, C. A., and Barreto, G. F., 1991, "Evaluation of Radiative Heat Transfer Properties in Dense Particulate Media," Powder Technol., **67**, pp. 137–144.

A Model of Heat and Mass Transfer Beneath an Ablating Concrete Surface

Michael Epstein
Fauske & Associates, Inc., 16W070 West 83rd Street, Burr Ridge, IL 60527

This paper presents a one-dimensional steady-state model of heat and water vapor transport just beneath an ablating concrete surface. In the model an evaporation front separates a dry porous region through which water vapor flows to the ablation front from a semi-infinite region that is partially wet with evaporable water. The predicted water vapor pressures at the evaporation front are quite high and could conceivably cause the concrete to spall. The model is quantitatively compatible with spallation events observed during tests involving the pouring of molten steel onto concrete and is capable of explaining the disparate results obtained in two rather extensive test series on the penetration of induction heated metallic pools into concrete. [DOI: 10.1115/1.1666884]

Keywords: Ablation, Decomposition, Heat Transfer, Porous Media, Vaporization

Introduction

Studies of postulated severe accidents in nuclear reactors have included consideration of the consequences of molten core debris draining from the reactor vessel onto the horizontal surface of the concrete foundation below the reactor vessel. Extensive experimental studies of the erosion rate of concrete by overlying molten steel were carried out at Sandia National Laboratory [1–3] and at Kernforshungszentrum Karlsruhe (KfK), Germany [see, e.g. [4],[5]]. In the KfK (so-called BETA) experiments and in the Sandia experiments the melt/concrete interaction was sustained by an induction heating coil placed around the interaction vessel. The metallic pool penetration rates measured in the BETA experiments were up to an order-of-magnitude higher than those reported by Sandia for similar pool temperatures and identical concrete substrates. In considering this discrepancy, for which no defensible explanation has yet been offered, it is proposed here that intense impingement heat transfer during the initial pouring of the steel melt from a relatively high elevation into the BETA test-section concrete cavity resulted in early, rapid concrete erosion. The erosion rate was so rapid that the free water in the concrete exerted a high vapor pressure just beneath the concrete surface which caused concrete surface spallation that wiped away the slag resistance to heat transfer. Once started, the rapid erosion rate was self-sustaining. Surface spallation did not occur in the inductively heated melt pools in the Sandia tests because the steel melt was either gradually generated in the test section or the pour stream was too short to initiate surface spallation.

A one-dimensional model is presented below that supports a spallation mechanism in the BETA tests, based on the presence of readily vaporized water and available measurements of the permeability of concrete as a function of temperature. Before the model is introduced it will prove useful to review early experiments involving steel melts poured onto concrete in the absence of an applied heat source [6], since concrete spallation was observed in these experiments.

Contributed by the Heat Transfer Division for publication in the JOURNAL OF HEAT TRANSFER. Manuscript received by the Heat Transfer Division November 22, 2002; revision received June 17, 2003. Associate Editor: J. N. Chung.

Experiments of Powers and Arellano

Early in the Sandia molten core debris-concrete interaction test program, exploratory experiments were performed in which steel melts were poured from an induction furnace into concrete crucibles [6]. These tests involved 200 kg steel melts initially heated to about 2000 K. The experiments were not well instrumented and no further heating was applied to the melt once it was poured on the concrete. The melts cooled to the steel solidification temperature in about 4 minutes. Each concrete crucible was used several times. The frozen mass of metal from a previous experiment was removed and another test was initiated in the eroded crucible. Motion picture records of the tests in which melts were poured into ''fresh'' concrete crucibles revealed concrete spallation events. The concrete spall fragments that escaped the crucible were collected and their thicknesses were found to vary from 2 to 7 mm. From the motion picture records the mean ejection velocity of limestone-type concrete fragments was determined to be about 5 $m\,s^{-1}$ while that of basaltic concrete was about 3.75 $m\,s^{-1}$.

Physical Model

A schematic diagram of the problem we wish to solve is presented in Fig. 1. It is assumed that the evaporable water held by the concrete is converted into vapor some distance below the ablating concrete surface. The vapor flows upward (in the negative x-direction) with superficial velocity j_g through hot porous concrete to the ablating surface where it is released to the overlying molten debris pool. Heat is conducted from the ablation front through the porous region to the plane of evaporation at $x=\delta_d$. The evaporation plane separates the dry porous region of thickness δ_d from the semi-infinite concrete region $x>\delta_d$ that is partially wet with evaporable water. At the evaporation front the water exerts an equilibrium pressure $P_{eq}(T_{\rm sat})$ at the local temperature $T_{\rm sat}$. The water vapor released at the plane of evaporation is transported across the porous region to the ablation front by the imposed pressure difference $P_{eq}(T_{\rm sat})-P_\ell$ where P_ℓ is the pressure in the overlying pool. The objective of the analysis is to compute the vapor pressure P_{eq} at the evaporation front.

The prediction of P_{eq} is based on the following set of simplifying assumptions which are examined more quantitatively in a subsequent section: (1) the ablation front propagates at a constant velocity v_m so that constant-pattern (steady-state) temperature

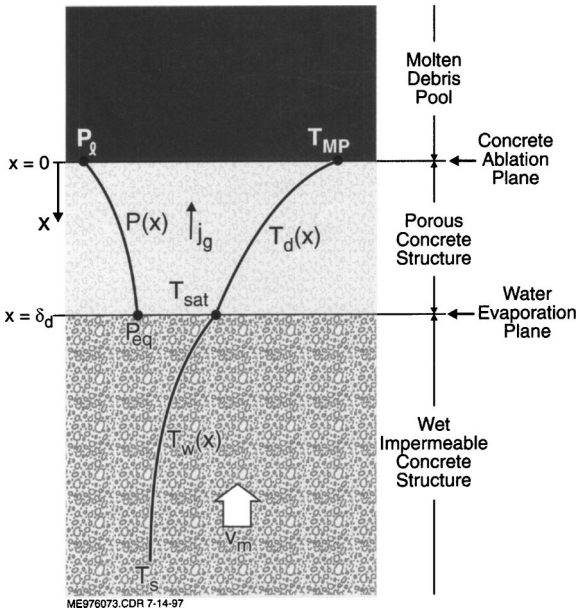

Fig. 1 Schematic diagram of concrete ablation model; indicating nomenclature and temperature and pressure profiles

profiles $T_d(x)$ and $T_w(x)$ are established in the dry and wet zones, respectively; (2) the evaporation plane is regarded as a sharp front that is very thin on the scale of the thickness of the porous region and the rate limiting process for concrete ''dehydration'' is taken to be water vapor convection (Darcy flow) through the porous layer between the water evaporation and concrete ablation fronts; (3) all the water vapor produced at the evaporation plane flows upward to the ablation front at the opposite end of the porous region; (4) forced and natural convection heat transfer in the porous region due to water vapor transport is negligible compared with conduction; (5) the pressure difference due to surface tension effects across the evaporation front is small compared to $P_{eq}-P_\ell$; and (6) the physical properties of the concrete and the viscosity μ_g of the water vapor may be replaced by constant average values appropriate to the temperature intervals of interest.

It is obvious from Assumption (1) that attention is focused on a one-dimensional system of coordinates in which the ablation front is at rest and the concrete medium moves with velocity v_m in the negative x-direction. The position of the ablation front is taken to be $x=0$.

Governing Equations

The conduction equation for the temperature profile $T_d(x)$ in the dry porous region of the translating concrete is

$$v_m\frac{dT_d}{dx}+a_d\frac{d^2T_d}{dx^2}=0;\quad 0<x<\delta_d \tag{1}$$

while the conduction equation for the temperature profile $T_w(x)$ in the region ''upstream'' of the evaporation plane, which is wet with evaporable water, is

$$v_m\frac{dT_w}{dx}+a_w\frac{d^2T_w}{dx^2}=0;\quad \delta_d<x<\infty \tag{2}$$

The momentum equation for the local mass-average velocity (superficial) j_g of the water vapor within the dry porous region is given by the differential form of Darcy's Law:

$$\frac{dP}{dx}=\frac{\mu_g j_g}{\kappa};\quad 0<x<\delta_d \tag{3}$$

In writing Eq. (3) the relative motion between the gas and the moving solid concrete was ignored since in all cases of interest $j_g\gg v_m$. The constant upward rate of water vapor mass flow through the porous region equals the rate at which vapor is generated at the evaporation plane:

$$\rho_w Y_g v_m=j_g\rho_g \tag{4}$$

The boundary conditions at the water evaporation plane $(x=\delta_d)$ are

$$\rho_w Y_g v_m h_{fg}=-k_d\frac{dT_d}{dx}+k_w\frac{dT_w}{dx};\quad x=\delta_d \tag{5}$$

$$T_d(\delta_d)=T_w(\delta_d)=T_{\text{sat}},\quad P(\delta_d)=P_{eq}(T_{\text{sat}}) \tag{6}$$

Equation (5) states that the energy required to evaporate the water is equal to the difference between the heat conducted in and out of the evaporation plane. At the ablation front $(x=0)$ and at $x=\infty$ the temperature and vapor pressure profiles must satisfy the conditions

$$T_d(0)=T_{mp},\quad P(0)=P_\ell,\quad T_w(\infty)=T_s \tag{7}$$

The model for evaporable water release from ablating concrete is complete with the addition of two equations. One equation is the ideal gas law for the vapor in the porous region, namely,

$$P=\rho_g R_g T_d \tag{8}$$

The other equation is for the permeability of the porous concrete region. The experimental measurements of McCormack et al. [7] show that the concrete permeability increases rapidly with temperature. Their data on the permeabilities of basaltic and limestone concretes were fit by the exponential function

$$\kappa=\kappa_0\exp(BT) \tag{9}$$

where the numerical values of the parameters κ_0 and B are given in Table 1. In the present problem the local concrete temperature may be as high as about 1600 K so that extrapolation of Eq. (9) would appear to be necessary. This issue will be discussed later on.

Table 1 Values of parameters in permeability equation (Eq. 9)

Concrete	Temp. Range (K)	κ_0 (m^2)	B (K^{-1})
Basaltic	373–900	2.18×10^{-17}	0.0110
Limestone	373–692	5.29×10^{-20}	0.0192
Limestone	692–1023	3.147×10^{-17}	0.01013

The solutions of Eqs. (1) and (2) that satisfy the relevant boundary conditions in Eqs. (5) to (7) give, after introducing the approximation $\rho_d c_d\cong\rho_w c_w$,

$$\frac{v_m\delta_d}{a_d}=\ln\left[1+\frac{T_{mp}-T_{\text{sat}}}{Y_g h_{fg}/c_w+T_{\text{sat}}-T_s}\right] \tag{10}$$

$$\frac{dT_d}{dx}=-\frac{v_m}{a_d}\left[T_d-T_s+\frac{Y_g h_{fg}}{c_w}\right] \tag{11}$$

Using Eq. (11) to eliminate independent distance variable x in Darcy's equation (Eq. 3) in favor of temperature T_d and by invoking Eqs. (4), (8), and (9), a separable first-order differential equation between pressure P and temperature T_d in the porous region of the concrete is obtained:

$$\frac{PdP}{dT_d}=-\frac{\mu_g a_d\rho_w Y_g R_g}{\kappa_0}\left(\frac{T_d}{T_d-T_s+Y_g h_{fg}/c_w}\right)\exp(-BT_d) \tag{12}$$

Equation (12) can be integrated between the ablation plane where $P=P_\ell$ and $T=T_{mp}$ and the evaporation plane where $P=P_{eq}$ and $T=T_{\text{sat}}$ to obtain the closed form result:

$$P_{eq}^2=P_\ell^2+\frac{2\mu_g a_d\rho_w Y_g R_g}{\kappa(T_s)B}\cdot f(T_{\text{sat}}) \tag{13}$$

where $\kappa(T_s)$ is Eq. (9) evaluated at T_s and the dimensionless function $f(T_{\text{sat}})$ is defined as

$$\begin{aligned}f(T_{\text{sat}})=&\exp[-B(T_{\text{sat}}-T_s+Y_g h_{fg}/c_w)]-\exp[-B(T_{mp}-T_s\\&+Y_g h_{fg}/c_w)]+B(T_\infty-Y_g h_{fg}/c_w)\{\text{Ei}[B(T_{\text{sat}}-T_s\\&+Y_g h_{fg}/c_w)]-\text{Ei}[B(T_{mp}-T_s+Y_g h_{fg}/c_w)]\}\end{aligned} \tag{14}$$

The function Ei[λ] in the above equation is the exponential integral

$$\text{Ei}[\lambda)]=\int_\lambda^\infty\frac{e^{-\xi}}{\xi}d\xi \tag{15}$$

Strictly speaking, Eqs. (13) and (14) are not valid for limestone concrete. The permeability versus temperature function for this material is composed of two exponentials connected in a piecewise continuous manner (see Eq. (9) and Table 1). Thus one would expect more terms to appear in Eqs. (13) and (14) involving two different κ_0, B pairs, one pair for the low temperature range 373–692 K and the other pair for the high temperature range 692 K to T_{mp}. It will be seen later on, however, that for the limestone concrete ablation problems considered here it is permissible to consider only one temperature range and, therefore, only one pair of κ_0, B values.

Equation (13) is a relationship between the two unknowns P_{eq} and T_{sat} at the evaporation front. Since thermodynamic equilibrium is assumed to prevail at the evaporation front the steam tables provide another relationship between P_{eq} and T_{sat} and the simultaneous numerical solution of these coupled relationships yields the pressure P_{eq} exerted by the vapor at the evaporation front. The actual numerical solution was performed using the following water vapor pressure fit of steam table data (to within 4.0 percent for $370 < T_{sat} < 584$ K):

$$P_{eq} = 10^6 \exp\left(-\frac{4795}{T_{sat}} + 10.55 \right) \tag{16}$$

where T_{sat} is in *K* and P_{eq} is in Pa.

The theory presented in the foregoing can also be used to calculate the pressure exerted by CO_2 gas within the concrete due to carbonate decomposition, providing that it is reasonable to regard the carbonate decomposition zone as a sharp front. Specifically, for the CO_2 case the water evaporation plane in Fig. 1 is replaced by a carbonate decomposition plane. In terms of obtaining numerical results with Eqs. (13) and (14) Y_g is now the mass fraction of CO_2 in the concrete, h_{fg} is identified with the heat of carbonate decomposition (decarboxylation), and R_g is the ideal gas constant for CO_2. Also, Eq. (16) is replaced by an equilibrium law for carbonate decomposition. Assuming CO_2 is produced in the concrete by the decarboxylation of calcium carbonate, we have

$$P_{eq} = 10^5 \exp\left(-\frac{2.085 \times 10^4}{T_{sat}} + 17.854 \right) \tag{17}$$

where P_{eq} is in Pa and T_{sat} is in *K*. Equation (17) is a fit to the saturation vapor pressure calculations for the reaction equilibrium $CaCO_3 = CaO + CO_2$. Assuming, instead, that CO_2 is produced from dolomite, $MgCa(CO_3)_2$, does not change the numerical results in a substantial way.

Discussion of Results

The physical property values used in the numerical solutions of Eqs. (13) and (16) for H_2O release and Eqs. (13) and (17) for CO_2 release are summarized in Table 2 (see also, Table 1). The thermophysical properties values of concrete were taken from [8]. Concrete does not melt at a single, sharp temperature. Rather it melts over a range. In the Sandia tests (see, e.g., [1]) the concrete ablation front was identified with the 1600 K isotherm as determined by thermocouples cast into the concrete substrate and this value is used here for T_{mp}.

The P_{eq} predictions are shown in Table 3 and they are compatible with the observations of Powers and Arellano [6]. We note that the driving pressure $P_{eq} - P_\ell$ for water flow in the limestone concrete is more than twice that in basaltic concrete, even though these concretes contain similar amounts of readily vaporized water (see Table 2). The reason for this difference is that the permeability of limestone concrete is about one order-of-magnitude less than the permeability of basaltic concrete [7]. The $P_{eq} - P_\ell$ results for H_2O are consistent with Powers and Arellano's observations of roughly 40 percent lower ejection velocities for basaltic concrete spall fragments relative to fragments ejected from limestone concretes. The ejection velocity can be shown to be proportional to $(P_{eq} - P_\ell)^{1/2}$, assuming that P_{eq} remains constant behind an ejecting spall fragment. The model results also confirm their conjecture that decarboxylation is not likely to be responsible for concrete spallation. The predicted low internal gas pressures associated with CO_2 release is a consequence of the fact that decarboxylation occurs in zones of high concrete temperatures having relatively high concrete permeabilities. A high-temperature porous concrete region offers little ''frictional'' resistance to the upward flow of CO_2 gas.

Table 2 Physical constants used in the numerical determinations of P_{eq}

Concrete Thermal Diffusivity	$a_d = 6.4 \times 10^{-7}$ m^2 s^{-1}
Gas Viscosity	$\mu_g = 2 \times 10^{-5}$ Pa s
Concrete Density	$\rho_w = 2340$ kg m^{-3}
Concrete Specific Heat	$c_w = 950$ J kg^{-1} K^{-1}
Ambient (Pool) Pressure	$P_\ell = 10^5$ Pa
H_2O Mass Fraction in Basaltic Concrete	$Y_g = 0.042$
H_2O Mass Fraction in Limestone Concrete	$Y_g = 0.039$
CO_2 Mass Fraction in Basaltic Concrete	$Y_g = 0.0292$
CO_2 Mass Fraction in Limestone Concrete	$Y_g = 0.357$
H_2O Heat of Evaporation	$h_{fg} = 2.2 \times 10^6$ J kg^{-1}
CO_2 Heat of Release	$h_{fg} = 3.8 \times 10^6$ J kg^{-1}
Ablation Temperature	$T_{mp} = 1600$ K
Cold Concrete Temperature	$T_s = 293$ K

Table 3 Predictions of equilibrium pressures exerted by the release of evaporable water and CO_2 in basaltic and limestone concretes

Concrete	Gas Released	Gas Mass Fraction	Predicted T_{sat} (K)	Predicted $P_{eq} - P_\ell$ (atm)
Basaltic	H_2O	0.042	409.6	2.13
Limestone	H_2O	0.039	436.5	5.46
Basaltic	CO_2	0.0292	1168.7	2.1×10^{-4}
Limestone	CO_2	0.357	1168.8	2.4×10^{-3}

The prediction $T_{sat} = 437$ K for limestone concrete is based only on the κ_0, *B* values in Table 1 for the low temperature range 373 to 692 K. For a change in temperature from 437 K to 692 K the permeability of limestone concrete increases by a factor of about 140. Thus practically all the resistance to upward water vapor flow in the porous region occurs close to the evaporation front and the precise values of the permeability at locations where the temperature is above 692 K are not important. Extrapolation of Eq. (9) to $T_{mp} = 1600$ K is indeed not required. Another way of stating this is that in Eq. (14) the terms containing T_{mp} are negligible compared with the terms containing T_{sat}. The predicted T_{sat} values for CO_2 gas release are outside and above the temperature range investigated by McCormack et al. [7] in their laboratory study of concrete permeability so that some extrapolation of Eq. (9) was required. However, any inaccuracies associated with this extrapolation does not alter the conclusion that the gas pressure generated by CO_2 release is negligible.

The fact that high-internal-water-vapor pressures are predicted by the model does not provide a complete explanation for the onset of spallation. If the plane of free water evaporation is far removed from the ablating surface, that is ''deep'' within the concrete, then it is reasonable to suppose that the concrete can withstand the few atmospheres of internal pressure produced by water release. However, spallation may occur if the zone of high pressure is just beneath the ablating surface. According to the observations of Powers and Arellano [6], the thicknesses of the spall fragments ranged in size from 2.0 to 7.0 mm. Thus a possible criterion for the onset of spallation is obtained by demanding that the thickness δ_d of the porous region of the concrete (see Fig. 1) be less than the largest measured spall fragment, denoted here as the critical size fragment $\delta_{d,crit} \cong 7.0$ mm. The criterion $\delta_d \cong \delta_{d,crit}$ can be combined with Eq. (10) for v_m to arrive at a critical ablation velocity $v_{m,crit}$, which if exceeded, results in spallation. Using the parameter estimates from Table 2 and the prediction $T_{sat} = 410$ K for basaltic concrete (see Table 3) in Eq. (10) leads to a threshold ablation velocity for spallation: $v_{m,crit} = 0.17$ mm s^{-1}. This value is consistent with the notion that spallation did not occur in the Sandia inductively heated pool tests but was important in most of the BETA tests in that the measured ablation rates in the Sandia tests fall well below this value while the ablation rates measured in the BETA tests are close to or exceed this value.

In all likelihood the mechanism of ablation is dictated early on during the melt pool formation stage. The BETA tests were initiated by pouring about 300 kg of steel melt into the interaction crucible from a height of several meters. Presumably the combination of intense impingement heat transfer, fresh concrete containing free water, and induction-heating power, led to the sustained, rapid concrete erosion rates measured in these tests. The rapid erosion process is achieved by concrete spallation which eliminates the slag resistance to heat transfer. In contrast, the inductively heated melt pools in the Sandia tests [2,3] developed gradually by melting at low power a solid steel cylinder initially placed in the interaction cavity. In these experiments the combination of low initial concrete heating rates and the possible loss of some free water by preheating of the concrete before the start of ablation prevented the possibility of spallation and concomitant rapid ablation. In the early transient cooldown tests performed at Sandia [6] spallation did not occur in concrete crucibles that were previously dried by exposure to steel melts. Note that this observation rules out a thermal stress mechanism of spallation. In the Sandia tests reported in [1] about 45 kg of steel melt was poured into the concrete crucible from a height of 1.0 m. Apparently the duration and intensity of the early stage melt-to-concrete heat transfer in these tests were limited by the relatively small melt mass poured and small pour height, compared with the melt mass and pour height in the BETA tests.

Discussion of Assumptions

In this section the validity of the assumptions underlying the model presented in the foregoing is examined. We begin with the assumption of steady-state ablation (Assumption 1).

In the BETA tests [4,5] the ablation front location was observed to vary linearly with time, starting from the first ablation depth measurement at about 10 s out to the end of the tests at about 400 s. It is apparent that steady-state catastrophic concrete erosion was established very quickly ($<$ 10 s). This observation is consistent with available solutions to the transient heat-conduction equation written for moving solids (see, e.g., [9]), from which the relaxation time t_{ss} to steady state is easily seen to be of the order

$$t_{ss} \sim \left(\frac{v_m^2}{4a_d} + \frac{\pi^2 a_d}{\delta_d} \right)^{-1} \tag{18}$$

Using the previous estimate $\delta_d \cong 7.0$ mm and the average ablation velocity measured in the BETA tests $v_m \cong 0.3\ \mathrm{mm\ s^{-1}}$, gives $t_{ss} \sim 6$ s.

Assumption (2) concerning the sharp boundary between the wet and dry zones is based on experimental measurements. Measured temperature histories at various depths below an ablating concrete surface exhibit discontinuities in slope when the concrete temperature rises to the boiling point of water [1]. The wet/dry line interface assumption has been used in previous theoretical studies of water evaporation or condensation in porous media (see, e.g., [10,11]).

Assumption (3) (negligible downward vapor transport) will be valid if

$$\frac{\delta_d \kappa(T_s)}{\delta_w \kappa(T_{\mathrm{sat}})} \ll 1.0 \tag{19}$$

In all the experiments cited here $\delta_d \ll \delta_w$. Also $\kappa(T_{\mathrm{sat}}) \cong 4.0\ \kappa(T_s)$, thereby assuring a negligible amount of downward vapor escape. Measurements of the concrete off-gas flow rates indicate that practically all of the gas stored in the concrete ($H_2O + CO_2$) is released to the overlying steel melt [3].

Forced-convection vapor heat transport in the dry region is negligible (Assumption 4) providing that (see Eq. (4))

$$\frac{\rho_g j_g c_g}{\rho_w v_m c_w} = \frac{Y_g c_g}{c_w} \ll 1.0 \tag{20}$$

Since $Y_g \ll 1.0$ for water (see Table 2) this inequality is indeed satisfied. Natural convection in the dry region can be neglected (Assumption 4) if the appropriately defined Rayleigh number,

$$\mathrm{Ra} = \frac{\kappa g \beta \delta_d (T_{mp} - T_{\mathrm{sat}})}{\alpha \nu_g}, \tag{21}$$

is small. The approximate values of the parameters in Eq. (21) are: $\kappa = 1.3 \times 10^{-12}\ \mathrm{m^2}$ [at $(T_{\mathrm{sat}} + T_{mp})/2 = 10^3$ K], $\beta = 2.4 \times 10^{-3}\ \mathrm{K^{-1}}$, $\delta_d = 7.0 \times 10^{-3}$ m, $T_{mp} - T_{\mathrm{sat}} = 1190$ K, $\alpha = 4.7 \times 10^{-4}\ \mathrm{m^2\ s^{-1}}$, and $\nu_g = 1.3 \times 10^{-5}\ \mathrm{m^2\ s^{-1}}$. These estimates yield $\mathrm{Ra} = 4.2 \times 10^{-5}$. It is well known that natural convection is negligible for $\mathrm{Ra} < 40.0$.

With respect to the influence of interfacial curvature on P_{eq} (Assumption 5), Satik and Yortsos [12] have shown that this effect is small unless the permeability of the porous medium is less than about $10^{-18}\ \mathrm{m^2}$. For the concrete materials and temperature ranges presented in this study $\kappa > 2 \times 10^{-16}\ \mathrm{m^2}$.

Concluding Remarks

Steel melts poured onto concrete may initiate a rapid concrete erosion process via the mechanism of concrete surface spallation by readily vaporized water. Concrete spallation was observed during the pouring of molten steel into concrete crucibles and prior to the cooldown of the metal. The present model of heat and water vapor transfer in the high temperature environment just beneath an ablating concrete surface rationalizes spallation observations during the transient cooldown tests and suggests that sustained spallation-driven concrete erosion occurred during experiments (BETA tests) in which the metal melt was continually heated after it was poured onto concrete. The present model can not predict whether or not a given metallic (or oxidic) pour will result in rapid concrete erosion by surface spallation. Such a prediction will require a new model which is capable of dealing with the transient period during which melt-pool heat transfer evolves from impingement heat transfer.

Nomenclature

- a = thermal diffusivity of concrete
- B = constant in permeability function, Eq. (9)
- c = specific heat of concrete
- c_g = specific heat of water vapor
- g = gravitational constant
- h_{fg} = latent heat of evaporation of water or heat of carbonate decomposition
- k = thermal conductivity of concrete
- j_g = superficial velocity of water vapor in dry porous region
- P = local water vapor pressure in dry porous region
- P_{eq} = equilibrium water vapor pressure at evaporation front
- P_ℓ = pressure in the overlying melt pool
- R_g = ideal gas constant for water
- t_{ss} = relaxation time to steady state
- T = local temperature
- T_{mp} = concrete melting (ablation) temperature
- T_s = temperature of wet concrete far from the evaporation plane
- T_{sat} = equilibrium (saturation) temperature at evaporation front
- v_m = concrete ablation velocity
- x = distance measured from ablation plane into concrete
- Y_g = mass fraction of evaporable water in wet concrete or mass fraction of CO_2 ''stored'' in concrete

Greek Letters

α = thermal diffusivity (concrete thermal conductivity divided by volumetric heat capacity of steam)
δ_d = thickness of dry porous region
δ_w = thickness of wet region
κ = local permeability of the dry porous region
κ_0 = permeability coefficient in Eq. (9)
μ_g = viscosity of water vapor
ν_g = kinematic viscosity of water vapor
ρ_g = local water vapor density in dry porous region
ρ_w = density of wet concrete

Subscripts

d = pertains to dry porous region
g = pertains to water vapor
w = pertains to wet region or liquid water

References

[1] Blose, R. E., Gronager, J. E., Suo-Anttila, A. J., and Brockmann, J. E., 1987, "SWISS: Sustained Heated Metallic Melt/Concrete Interactions with Overlying Pools," Sandia National Lab. Report SAND85-1546 (NUREG/CR-4727).
[2] Copus, E. R., Blose, R. E., Brockmann, J. E., Gomez, R. D., and Lucero, D. A., 1990, "Experimental Results of Core-Concrete Interactions Using Molten Steel with Zirconium," Sandia National Laboratory Report SAND86-2638 (NUREG/CR-4794).
[3] Copus, E. R., Blose, R. E., Brockmann, J. E., Gomez, R. D., and Lucero, D. A., 1989, "Core-Concrete Interactions Using Molten Steel with Zirconium on a Basaltic Basemat: The SURC-4 Experiment," Sandia National Laboratory Report SAND87-2008 (NUREG/CR-4994).
[4] Corradini, M., and Reineke, H. H., 1989, "A Review of the BETA Experimental Results and Code Comparison Calculations," Nucl. Sci. Eng., **102**, pp. 260–282.
[5] Alsmeyer, H., 1995, "Review of Experiments on Dry Corium Concrete Interaction," in *Molten Corium/Concrete Interaction and Corium Coolability—A State of the Art Report*, European Commission, Brussels, Report EVR 16649 EN, pp. 29–82.
[6] Powers, D. A., and Arrellano, F. E., 1982, "Large-Scale, Transient Tests of the Interaction of Molten Steel with Concrete," Sandia National Laboratory Report SAND81-1753 (NUREG/CR-2282).
[7] McCormack, J. D., Postma, A. K., and Schur, J. A., 1979, "Water Evolution from Concrete," Hanford Engng. Dev. Lab., Report HEDL-TME 78–87.
[8] Kao, L. S., and Kazimi, M. S., 1987, "Thermal Hydraulics of Core/Concrete Interactions in Severe LWR Accidents," MIT Report MITNE-276.
[9] Carslaw, H. S., and Jaeger, J. C., 1959, *Conduction of Heat in Solids*, 2nd ed., Oxford Univ. Press, p. 391.
[10] Rubin, A., and Schweitzer, S., 1972, "Heat Transfer in Porous Media with Phase Change," Int. J. Heat Mass Transfer, **15**, pp. 43–59.
[11] Chung, M., and Catton, I., 1993, "Steam Injection into a Slow Water Flow Through Porous Media," ASME J. Heat Transfer, **115**, pp. 734–743.
[12] Satik, C., and Yortsos, Y. C., 1991, "Percolation Models for Boiling and Bubble Growth in Porous Media at Low Superheats," in *Multiphase Transport in Porous Media*, FED-Vol. 122/HTD-Vol. 186, ASME, New York, pp. 61–72.

Investigation of the Initial Inverse Problem in the Heat Equation

Khalid Masood
e-mail: masood@kfupm.edu.sa
Hafr Al-Batin Community College, King Fahd University of Petroleum and Minerals, P.O. Box 5087, Dhahran 31261, Saudi Arabia

F. D. Zaman
e-mail: fzaman@kfupm.edu.sa
Department of Mathematical Sciences, King Fahd University of Petroleum and Minerals, Dhahran 31261, Saudi Arabia

We investigate the inverse problem in the heat equation involving the recovery of the initial temperature from measurements of the final temperature. This problem is extremely ill-posed and it is believed that only information in the first few modes can be recovered by classical methods. We will consider this problem with a regularizing parameter which approximates and regularizes the heat conduction model. [DOI: 10.1115/1.1666886]

Keywords: Analytical, Heat Transfer, Inverse, Stability, Temperature

1 Introduction

The classical direct problem in heat conduction is to determine the temperature distribution of a body as the time progresses. The task of determining the initial temperature distribution from the final distribution is distinct from the direct problem and is identified as the initial inverse heat conduction problem. This type of inverse problem is extremely ill-posed, e.g., Engle [1]. There is an alternative approach which consists of a reformulation of the classical heat equation by a hyperbolic heat equation (see Weber [2], Elden [3], and Masood et al. [4]).

We will present an alternative approach which approximates and regularizes the initial inverse heat conduction solution. The need to consider the alternative formulation has some physical advantages. In many applications, one encounters a situation where the usual parabolic heat equation does not serve as a realistic model. Since the speed of propagation of the thermal signal is finite, e.g., for short-pulse laser applications, the hyperbolic differential equation correctly models the problem; see Vedavarz et al. [5] and Gratzke et al. [6] among others. The initial inverse problem in the hyperbolic heat equation is stable and well posed. Moreover, numerical methods for hyperbolic problems are efficient and accurate. We will utilize the small value of the parameter and apply the WKBJ (Wentzel, Kramers, Brillouin, and Jeffreys) method to solve the initial inverse problem, see Bender and Orszag [7].

2 Initial Inverse Problem in the Heat Equation

Supposing we have a metal bar, which for the sake of convenience we take to extend over the interval $0 \leqslant x \leqslant \pi$, whose temperature at the point x and at time t is given by the function $u(x,t)$. Then, for an appropriate choice of units, $u(x,t)$ satisfies the equation

$$\frac{\partial u}{\partial t} = \frac{\partial^2 u}{\partial x^2}, \quad 0 < x < \pi, \quad t > 0 \tag{1}$$

with homogeneous Dirichlet boundary conditions

$$u(0,t) = u(\pi,t) = 0 \tag{2}$$

We assume the final temperature distribution of the bar at time $t = T$

$$f(x) = u(x,T) \tag{3}$$

and we want to recover the initial temperature profile of the bar

$$g(x) = u(x,0) \tag{4}$$

The condition (2) can be replaced by an insulated boundary, i.e., $u_x(0,t) = u_x(\pi,t) = 0$, since it is important in some applications, see for example Beck et al. [8] and Al-Khalidy [9].

We assume by the separation of the variables, the solution of the direct problem of the form

Contributed by the Heat Transfer Division for publication in the JOURNAL OF HEAT TRANSFER. Manuscript received by the Heat Transfer Division May 15, 2002; revision received August 14, 2003. Associate Editor: A. F. Emery.

$$u(x,t)=\sum_{n=1}^{\infty} v_n(t)\phi_n(x) \tag{5}$$

The eigenfunctions of d^2/dx^2 given by $\phi_n(x)\doteq\sqrt{2/\pi}\sin(nx)$ form a complete orthonormal system in $L^2[0,\pi]$. Thus, $g(x)\in L^2[0,\pi]$ can be expanded as

$$g(x)=\sum_{n=1}^{\infty} c_n\phi_n(x), \quad x\in[0,\pi] \tag{6}$$

So, we can write the solution of the direct problem (1) in the form

$$u(x,t)=\sum_{n=1}^{\infty} c_n \exp[-n^2t]\phi_n(x) \tag{7}$$

Now by applying (3), we can write

$$f(x)=\int_0^{\pi} K(x,\zeta)g(\zeta)d\zeta \tag{8}$$

which is an integral equation of the first kind. The singular system of the integral Eq. (8) is given by

$$\{\exp[-n^2T],\phi_n(x),\phi_n(x)\} \tag{9}$$

Now by application of Picard's theorem the inverse problem can be solved if

$$\sum_{n=1}^{\infty} \exp[2n^2T]|f_n|^2<\infty \tag{10}$$

where

$$f_n=\int_0^{\pi}\phi_n(\zeta)f(\zeta)d\zeta \tag{11}$$

are the classical Fourier coefficients of f. Now again using Picard's theorem, we can recover the initial profile by the following expression

$$g(x)=\sum_{n=1}^{\infty} \exp[n^2T]f_n\phi_n(x) \tag{12}$$

Picard's theorem demonstrates the ill-posed nature of the problem considered. If we perturb the data by setting $f^{\delta}=f+\delta\phi_n$ we obtain a perturbed solution $g^{\delta}=g+\delta\phi_n\exp[n^2T]$. Hence, the ratio $\|g^{\delta}-g\|/\|f^{\delta}-f\|=\exp[n^2T]$ can be made arbitrarily large due to the fact that the singular values $\exp[-n^2T]$ decay exponentially. The influence of errors in the data f is obviously affected by the rate of this decay. So in regularizing, we will confine ourselves to lower modes by only retaining the first few terms in the series (12). This technique of truncating the series is known as truncated singular value decomposition (TSVD), see Hansen [10].

3 The Hyperbolic Model

The method we apply is similar to the quasi-inverse method of Lions [11]. The Lions' method is based on replacing the problem (1–4) by a problem for equation of higher order with a small parameter. There are several methods for solving ill-posed problems. The quasi-solution method to solve the equation of the first kind was introduced by Ivanov [12]. The essence of this method is to change the notion of solution of an ill-posed problem so that, for certain conditions, the problem of its determination will be well-posed. Tikhonov's regularization method is widely used for solving linear and nonlinear operator equations of the first kind, see Tikhonov and Arsenin [13]. Iterative methods are applied to solve different problems and particularly these methods can also be applied to solve operator equations of the first kind. Moultanovsky [14] applied such an iterative method to solve an initial inverse heat transfer problem. The projective methods for solving various ill-posed problems are based on the representation of the approximate solution as a finite linear combination of a certain functional system, see, e.g., Vasin and Ageev [15].

The methods mentioned in the previous paragraph may be applied for solving the extensive class of inverse problems. These methods do not take into account the specific character of concrete inverse problems. The Lion's method and the method we present in this paper take into account peculiarities of the inverse problem. There is an alternative approach to the inverse heat conduction problem [2,3], which consists of introducing a small damping parameter with the term $\partial^2u/\partial t^2$. So, let us consider the following hyperbolic heat equation

$$\epsilon\frac{\partial^2u}{\partial t^2}+\frac{\partial u}{\partial t}=\frac{\partial^2u}{\partial x^2}, \quad \epsilon>0, \quad 0<x<\pi, \tag{13}$$

together with conditions (2–4) and one additional condition

$$\frac{\partial u}{\partial t}(x,0)=0. \tag{14}$$

Following the same procedure as that for the parabolic heat equation and assuming the solution of the form (5), for $\epsilon\to0^+$ we get the following ordinary differential equation

$$\epsilon\frac{d^2a_n(t)}{dt^2}+\frac{da_n(t)}{dt}+n^2a_n(t)=0, \quad \epsilon>0, \quad t>0, \tag{15}$$

subject to

$$a_n(0)=c_n, \quad \text{and} \quad \frac{da_n(0)}{dt}=0. \tag{16}$$

This is a singular perturbation problem, so we seek the WKBJ solution to this problem [7]. The WKBJ solution to (15) is

$$a_n(t)=\left(\frac{\epsilon n^2-1}{2\epsilon n^2-1}\right)c_n\exp[-n^2t]+\left(\frac{\epsilon n^2c_n}{2\epsilon n^2-1}\right)\exp\left[n^2t-\frac{t}{\epsilon}\right] \tag{17}$$

Using Picard's theorem the solution exists if

$$\sum_{n=1}^{\infty}\frac{|f_n|^2}{\left\{\left(\frac{\epsilon n^2-1}{2\epsilon n^2-1}\right)\exp[-n^2T]+\left(\frac{\epsilon n^2}{2\epsilon n^2-1}\right)\exp\left[n^2T-\frac{T}{\epsilon}\right]\right\}^2}<\infty \tag{18}$$

and the solution is given by

$$g(x)=\sum_{n=1}^{\infty}\times\frac{f_n\phi_n(x)}{\left\{\left(\frac{\epsilon n^2-1}{2\epsilon n^2-1}\right)\exp[-n^2T]+\left(\frac{\epsilon n^2}{2\epsilon n^2-1}\right)\exp\left[n^2T-\frac{T}{\epsilon}\right]\right\}} \tag{19}$$

Supposing $\epsilon\to0^+$ in the expression (19), we get the solution of the heat conduction problem (12). So, the solution of the heat equation can also be treated as the limiting case of the hyperbolic heat equation.

Example. Let us consider the initial temperature distribution of the form $g(x)=\sqrt{2/\pi}\sin(mx)$, where m is some fixed integer, then the final data for (19) and (12) can be given by

$$f_m=\left(\frac{\epsilon m^2-1}{2\epsilon m^2-1}\right)\exp[-m^2T]+\left(\frac{\epsilon m^2}{2\epsilon m^2-1}\right)\exp\left[m^2T-\frac{T}{\epsilon}\right] \tag{20}$$

and

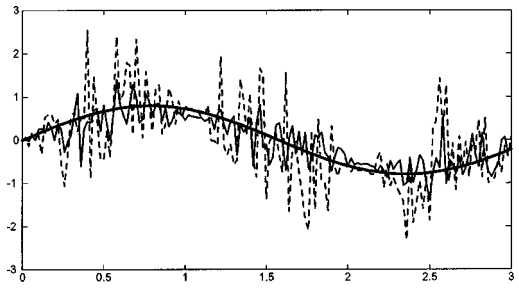

Fig. 1 The case of noisy data with SNR=50 dB, $N=3$, $m=2$, $T=1$, and $\epsilon=0.04$. The noisy data used in the heat conduction solution (12) is represented by the dotted line and in the damped wave solution (19) by the thin solid line and the noiseless temperature by the thick solid line.

$$f_m = \exp[-m^2 T]. \tag{21}$$

The expression (20) represents the final data for the hyperbolic model corresponding to the assumed initial profile $g(x)$ in the absence of the noise. Using (20) in the expression (19), the initial profile $g(x)$ can be recovered exactly. The expression (21) represents the final data for the parabolic model corresponding to the assumed initial profile $g(x)$ in the absence of the noise and the initial profile can be recovered exactly by using it in the expression (12).

Now we analyze the models by adding white Gaussian noise to the data (21). The reason to use (21) as final data is that the exact measured data would be of this form. In Figs. 1–3, we use the noisy data (white Gaussian noise+(21)) in both parabolic heat conduction and hyperbolic heat models and see the mean behavior of 100 independent realizations.

We have considered the second mode, that is, $m=2$ in Figs. 1–3 as well as retaining the first three terms ($N=3$) in series (12) and (19). In Fig. 1, the hyperbolic heat model behaves better than the parabolic heat conduction model for SNR=50 dB. We have increased the level of noise in Figs. 2–3 to SNR=20 dB. The inherent instability of the parabolic heat conduction model is clear from Fig. 3 by observing the range of the vertical axis.

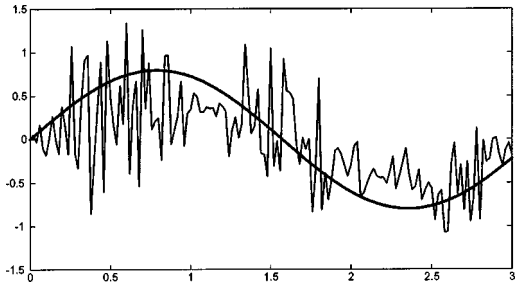

Fig. 2 Response of the damped model (19) in the case of noisy data with SNR=20 dB, $N=3$, $m=2$, $T=1$, $\epsilon=0.07$

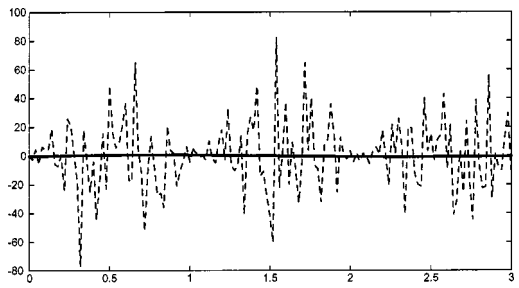

Fig. 3 Response of the classical heat model (12) in the case of noisy data with SNR=20 dB, $N=3$, $m=2$, $T=1$

Conclusions

The inverse solution of the heat conduction model is characterized by discontinuous dependence on the data. It is shown that in case of noisy data, the hyperbolic model approximates the exact initial profile better than the parabolic heat conduction model. Further, in the case of noisy data, the information about the initial profile cannot be recovered for higher modes by the parabolic heat conduction model but by the hyperbolic model some useful information may be recovered. However for higher modes the information recovered by the hyperbolic model is better than the parabolic model but it may not be good enough for a particular application.

Acknowledgment

The authors wish to acknowledge support provided by the King Fahd University of Petroleum and Minerals and the Hafr Al-Batin Community College.

Nomenclature

$|\cdot|$ = absolute value
$\|\cdot\|$ = norm
c_n = $\int_0^\pi g(x)\phi_n(\tau)d\tau$
$K(x,\zeta)$ = $\Sigma_{n=1}^{\infty} \exp[-n^2T]\phi_n(\zeta)\phi_n(x)$
u_x = $\partial u/\partial x$
SNR = signal-to-noise ratio
WKBJ = Wentzel, Kramers, Brillouin, and Jeffreys
$\phi_n(x)$ = eigenfunctions

References

[1] Engl, H. W., Hanke, M., and Neubauer, A., 1996, *Regularization of Inverse Problems*, Kluwer, Dordrecht, pp. 31–42.
[2] Weber, C. F., 1981, "Analysis and Solution of the Ill-Posed Problem for the Heat Conduction Problem," Int. J. Heat Mass Transfer, **24**, pp. 1783–1792.
[3] Elden, L., 1987, *Inverse and Ill-Posed Problems*, Engl, H. W., and Groetsch, C. W., eds., Academic Press, Inc., pp. 345–350.
[4] Masood, K., Messaoudi, S., and Zaman, F. D., 2002, "Initial Inverse Problem in Heat Equation With Bessel Operator," Int. J. Heat Mass Transfer, **45**(14), pp. 2959–2965.
[5] Vedavarz, A., Mitra, K., and Kumar, S., 1994, "Hyperbolic Temperature Profiles for Laser Surface Interactions," J. Appl. Phys., **76**(9), pp. 5014–5021.
[6] Gratzke, U., Kapadia, P. D., and Dowden, J., 1991, "Heat Conduction in High-Speed Laser Welding," J. Appl. Phys., J. Phys. D, **24**, pp. 2125–2134.
[7] Bender, C. M., and Orszag, S. A., 1978, *Advanced Mathematical Methods for Scientists and Engineers*, McGraw Hill, New York, Chap. 10.
[8] Beck, J. V., Blackwell, B., and Clair, C. A. St., 1985, *Inverse Heat Conduction Problems*, Wiley, New York.
[9] Al-Khalidy, N., 1998, "On the Solution of Parabolic and Hyperbolic Inverse Heat Conduction Problems," Int. J. Heat Mass Transfer, **41**, pp. 3731–3740.
[10] Hansen, P. C., 1997, *Rank-Deficient and Discrete Ill-Posed Problems*, SIAM, Philadelphia, PA, Chap. 3.
[11] Lions, J.-L., and Lattes, R., 1967, *Méthode de Quasi-réversibilité et Applications*, Dunod, Paris.
[12] Ivanov, V. K., 1963, "On Ill-Posed Problems," Mat. Sb., **61**(2), pp. 211–223 (in Russian).
[13] Tikhonov, A. N., and Arsenin, V. Ya., 1977, *Solution of Ill-Posed Problems*, John Wiley, New York.
[14] Moultanovsky, A. V., 2002, "Mobile HVAC System Evaporator Optimization and Cooling Capacity Estimation by Means of Inverse Problem Solution," Inverse Problems in Engng., **10**(1), pp. 1–18.
[15] Vasin, V. V., and Ageev, A. L., 1995, *Ill-Posed Problems With a Priori Information*, VSP, Utrecht.

Effect of Double Stratification on Free Convection in a Darcian Porous Medium

P. V. S. N. Murthy
e-mail: pvsnm@maths.iitkgp.ernet.in
Department of Mathematics, Indian Institute of Technology, Kharagpur 721 302, W.B., India

D. Srinivasacharya and P. V. S. S. S. R. Krishna
Department of Mathematics and Humanities, National Institute of Technology, Warangal, 506 004, A.P., India

The problem of free convection heat and mass transfer from vertical surface embedded in a doubly stratified porous medium has been studied. The similarity solution is presented for the case of uniform heat and mass flux conditions when the thermal and solutal stratification of the medium are assumed to have the power function form $x^{1/3}$. The flow, temperature and concentration fields are effected by the complex interactions among the diffusion ratio parameter Le and buoyancy ratio parameter N in addition to the flow driving Darcy-Rayleigh number Ra_x. The temperature and concentration profiles are effected due to double stratification of the medium and its effect on the Nusselt and Sherwood numbers is discussed. [DOI: 10.1115/1.1667525]

Keywords: Boundary Layer, Heat Transfer, Mass Transfer, Natural Convection, Porous Media, Stratified

1 Introduction

Thermal and solutal transport by fluid flowing through a porous matrix is a phenomenon of great interest from both theory and application point of view. Heat transfer studies in fluid saturated porous media have given insight into understanding dynamics of hot underground springs, terrestrial heat flow through aquifer, hot fluid and ignition front displacements in reservoir engineering, heat exchange between soil and atmosphere, flow of moisture through porous industrial materials, and heat exchanges with fluidized beds. Mass transfer studies have applications in miscible displacements in oil reservoirs, spreading of solutes in fluidized beds and crystal washers and salt leaching in soils. Prevention of salt dissolution into the lake water near sea shores has become a serious topic of research.

Applications are discussed with reference to salt and heat transport in porous flows in Ludvigsen et al. [1] and in Gilman and Bear [2]. Due to the applicability of these studies in many geotechnical processes, it is vital to have good theoretical understanding of the processes occurring in double diffusive flows in porous media. Interesting effects arise as the diffusion rates of heat and solute are usually different. Free convection heat and mass transfer from a vertical flat plate embedded in an unstratified porous medium has been thoroughly investigated in the recent past by many researchers such as Cheng [3], Bejan and Khair [4], Lai and kulacki [5], and Trevisan and Bejan [6]. The book by Nield and Bejan [7] covers many of the latest developments concerning double diffusive convection in a saturated porous medium.

Contributed by the Heat Transfer Division for publication in the JOURNAL OF HEAT TRANSFER. Manuscript received by the Heat Transfer Division July 17, 2002; revision received October 14, 2003. Associate Editor: V. Prasad.

Although the effect of stratification of the medium on the heat removal process in a porous medium is important, very little work has been reported in the literature. Bejan [8], Singh and Sharma [9], and Kalpana and Singh [10] studied the problem of boundary layer free convection along an isothermal vertical flat plate immersed in a thermally stratified fluid saturated porous medium using integral and series solution techniques. The case of power law variation of wall temperature with thermal stratification of the medium was discussed at length by Nakayama and Komaya [11] and by Lai et al. [12]. Takhar and Pop [13] investigated the free convective transport from a vertical flat plate in a thermally stratified Darcian fluid where the ambient temperature varies as $x^{1/3}$ using the similarity solution technique.

In practical situations where the heat and mass transfer mechanisms run in parallel, particularly in porous media applications, it is worth analysing the effect of double stratification (stratification of the medium with respect to the thermal and concentration fields) on the free convective heat and mass transfer in porous media. In the present paper, we extend the work of Takhar and Pop [13] to uncover the effect of double stratification on free convection heat and mass transfer in a Darcian fluid saturated porous medium using the similarity solution technique.

2 Governing Equations

Free convection heat and mass transfer from an impermeable vertical flat wall in a stable and doubly stratified fluid saturated porous medium is considered for study, the schematic drawing is shown in Fig. 1. The wall is maintained at constant heat and mass flux conditions q_w and q_m respectively. The temperature and the mass concentration of the ambient medium are assumed to be in the form $T_\infty(x)=T_{\infty,0}+Ax^{1/3}$, $C_\infty=C_{\infty,0}+Bx^{1/3}$ where $T_{\infty,0}$ and $C_{\infty,0}$ are the temperature and concentration at any reference point inside the boundary layers respectively. We also assume that the flow is slow such that the Darcy law is valid. Then the governing equations for the boundary layer flow, heat and mass transfer from the wall $y=0$ into the fluid saturated stratified porous medium $x \geqslant 0$ and $y>0$ (after making use of the Boussinesq approximation) are given by (see Nield and Bejan [7])

$$\frac{\partial u}{\partial x}+\frac{\partial v}{\partial y}=0 \tag{1}$$

$$u=\frac{Kg}{\nu}\{\beta_T(T-T_\infty)+\beta_C(C-C_\infty)\} \tag{2}$$

$$u\frac{\partial T}{\partial x}+v\frac{\partial T}{\partial y}=\alpha\frac{\partial^2 T}{\partial y^2} \tag{3}$$

$$u\frac{\partial C}{\partial x}+v\frac{\partial C}{\partial y}=D\frac{\partial^2 C}{\partial y^2} \tag{4}$$

with the boundary conditions

$$\left.\begin{array}{lll} y=0: v=0, & -k\dfrac{\partial T}{\partial y}=q_w, & -D\dfrac{\partial C}{\partial y}=q_m \\ y\to\infty: u\to 0, & T=T_\infty(x), & C=C_\infty(x) \end{array}\right\}. \tag{5}$$

Here x and y are the Cartesian coordinates, u and v are the averaged velocity components in x and y directions respectively, T is the temperature, C is the concentration, β_T is the coefficient of thermal expansion, β_C is the coefficient of solutal expansion, ν is the kinematic viscosity of the fluid, K is the permeability, g is the acceleration due to gravity. The subscripts w and ∞ indicate the conditions at the wall and at the outer edge of the boundary layer, respectively.

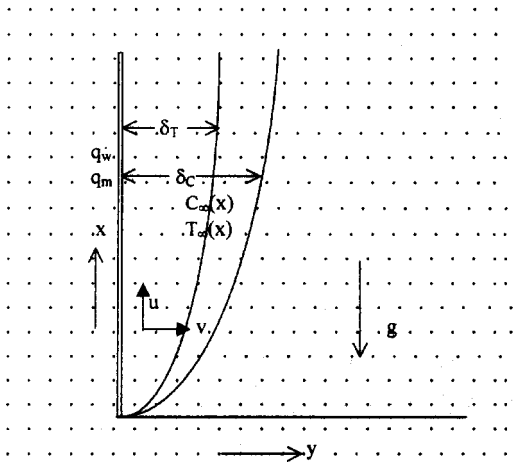

Fig. 1 Schematic drawing of the problem

Making use of the following similarity transformation

$$\eta = \frac{y}{x}\mathrm{Ra}_x^{1/3}, \quad \psi(\eta) = \alpha \mathrm{Ra}_x^{1/3} f(\eta),$$

$$T - T_\infty(x) = \frac{q_w x}{k}\mathrm{Ra}_x^{-1/3}\theta(\eta) \quad C - C_\infty(x) = \frac{q_m x}{D}\mathrm{Ra}_x^{-1/3}\phi(\eta)$$

the governing Eqs. (1–4) become,

$$f' = \theta + N\phi \tag{6}$$

$$\theta'' = \frac{1}{3}(\theta f' - 2f\theta' + \epsilon_1 f') \tag{7}$$

$$\phi'' = \frac{\mathrm{Le}}{3}(\phi f' - 2f\phi' + \epsilon_2 f') \tag{8}$$

and the boundary conditions (5) transform into

$$\left.\begin{aligned} \eta = 0 &: f = 0, \quad \theta' = -1, \quad \phi' = -1 \\ \eta \to \infty &: f' = 0, \quad \theta \to 0, \quad \phi \to 0 \end{aligned}\right\} \tag{9}$$

The important parameters involved are the local Darcy-Rayleigh number $\mathrm{Ra}_x = Kg\beta_T q_w x^2/\alpha\nu k$ which is defined with reference to the thermal conditions alone, the buoyancy ratio is $N = \beta_C q_m k/\beta_T q_w D$ and the diffusivity ratio $\mathrm{Le} = \alpha/D$. The Lewis number is the ratio of Schmidt number (ν/D) and Prandtl number (ν/α). $N > 0$ indicates the aiding buoyancy and $N < 0$ indicates the opposing buoyancy. The Stratification parameters are defined as $\epsilon_1 = k/q_w \mathrm{Ra}_x^{1/3}\partial T_\infty(x)/\partial x$ and $\epsilon_2 = D/q_m \mathrm{Ra}_x^{1/3}\partial C_\infty(x)/\partial x$. When $T(\infty)(x) = T_{\infty,o} + Ax^{1/3}$ and $C(\infty)(x) = C_{\infty,o} + Bx^{1/3}$, ϵ_1 and ϵ_2 will be independent of x and allows the similarity solution.

3 Results and Discussion

The resulting ordinary differential Eqs. (6–8) along with the boundary conditions (9) are integrated by giving appropriate initial guess values for $f'(0)$, $\theta(0)$, and $\phi(0)$ to match the values with the corresponding boundary conditions at $f'(\infty)$, $\theta(\infty)$, and $\phi(\infty)$, respectively. NAG software (D02HAFE routine) is used for integrating the corresponding first order system of equations and for shooting and matching the initial and boundary conditions. The integration length η_∞ varies with parameter values and it has been suitably chosen at each time such that the boundary conditions at the outer edge of the boundary layer are satisfied. The results obtained here are accurate up to fourth decimal place. Extensive calculations have been performed to obtain the flow, temperature and concentration fields for the following range of parameters: $-1 < N \leq 5$, $0.01 \leq \mathrm{Le} \leq 100$, $0 \leq \epsilon_1 \leq 5$ and $0 \leq \epsilon_2 \leq 5$. As an indication of proper formulation and accurate calculation, the results obtained here are compared with the results in Takhar and Pop [13].

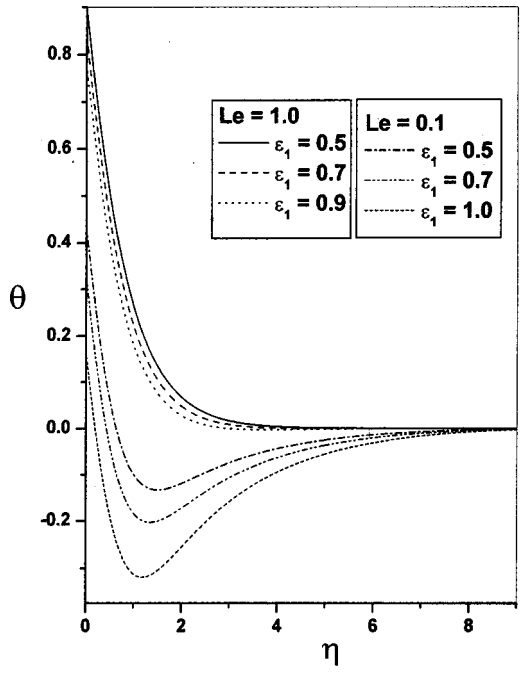

Fig. 2 Variation of temperature with η for different values of ϵ_1 when $N = 1$ and $\epsilon_2 = 0.3$

The effect of ϵ_1 and ϵ_2 on the wall velocity, temperature and concentration fields for uniform wall heat and mass flux conditions is plotted for some selected combinations of parameter values. For fixed value of $N(=1)$ and for Le=0.1, 1.0 variation of

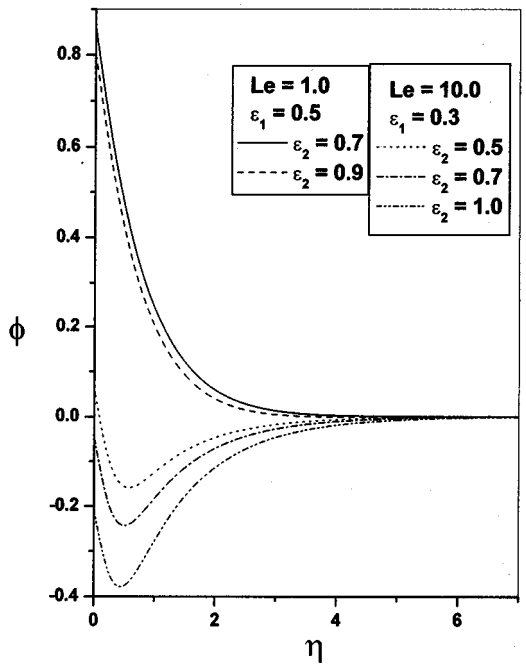

Fig. 3 Variation of concentration with η for different values of ϵ_2 when $N = 1$

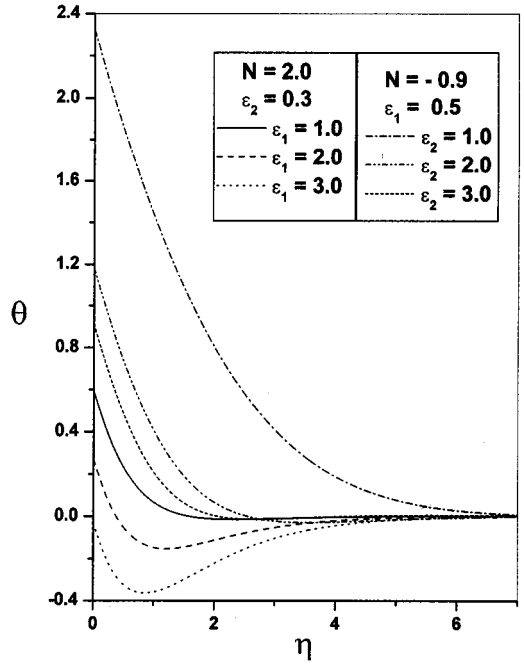

Fig. 4 Variation of temperature with η when Le=1

$\theta(\eta)$ with η is plotted in Fig. 2 for different values of ϵ_1 with $\epsilon_2=0.3$. Similarly variation of $\phi(\eta)$ with η is plotted in Fig. 3 for different values of ϵ_2 with $N=1$, Le=1.0, 10.0 and $\epsilon_1=0.3$, 0.5. The velocity and temperature at the wall decreased as the thermal stratification parameter ϵ_1 increased while the wall concentration decreased with an increase in the value of solutal stratification parameter ϵ_2. Increase in the value of solutal stratification parameter ϵ_2 further reduced the wall velocity and the wall temperature coefficients.

It is observed that the temperature and concentration profiles became negative from critical points η_T, η_C for temperature and concentration profiles, respectively, near the edge of the corresponding boundary layers before they finally attained the boundary conditions $\theta(\infty))=0$ and $\phi(\infty)=0$. Also, η_T shifts towards the wall as ϵ_1 becomes large and η_C shifts towards the wall as ϵ_2 is increased. This can be explained by the way in which the temperature and concentration fields are defined. We have

$$T-T_\infty(x)=\frac{q_w x}{k}\mathrm{Ra}_x^{-1/3}\theta(\eta)$$

and when the temperature in the medium becomes smaller than that of the stratified ambient medium, i.e., if $T-T_\infty(x)<0$, then $\theta(\eta)$ has to be negative as $q_w x/k\mathrm{Ra}_x^{-1/3}$ is positive. Similarly,

$$C-C_\infty(x)=\frac{q_m x}{D}\mathrm{Ra}_x^{-1/3}\phi(\eta),$$

$\phi(\eta)$ has to become negative when $C-C_\infty(x)<0$. In double diffusive processes in porous media, it is not unnatural to assume that different strata of the medium are at varying stratification levels and complex interactions among thermal and solutal fields can not be overruled. Also, overpowering of thermal stratification over the concentration stratification and vice versa resulted in interesting observations in the thermal and concentration profiles as discussed in this article. For fixed values of N and Le, when $\epsilon_1 \geqslant \epsilon_2$, $\theta(\eta)$ is becoming negative and when $\epsilon_2 \geqslant \epsilon_1$, $\phi(\eta)$ is becoming negative. This is also clear from the Figs. 2 and 3.

Now the effect of Le and N on the thermal and concentration profiles is as follows: Le<1 means $\alpha<D$ and mass diffusion is predominant. Hence the concentration profile decreases to zero without any change of sign in the boundary layer. In Fig. 2, the temperature profile is plotted for $N=1$, Le=0.1, $\epsilon_2=0.3$ and varying ϵ_1, in this case, the negative values are no more mild, and they creep into the boundary layer. Keeping ϵ_1 fixed at 0.3 and varying ϵ_2 is also resulting in a similar phenomena, but the temperature on the wall is increasing as ϵ_2 is increased and when $\epsilon_2 \gg \epsilon_1$ the temperature distribution is becoming free from the oscillations in the boundary layer. The temperature profile is plotted for large value of the buoyancy parameter in Fig. 4. A close observation of Figs. 2 and 4 clearly indicate that the oscillations are delayed by increasing the value of the buoyancy parameter. When $N<0$, the thermal field is stable with increasing values of

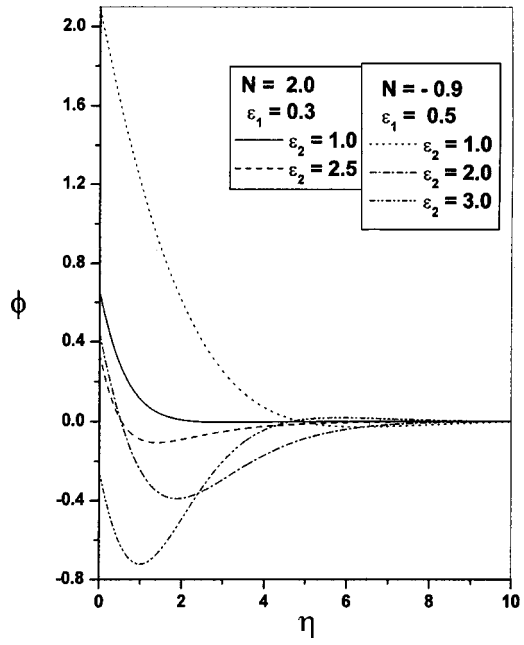

Fig. 5 Variation of concentration with η for different values of ϵ_2, when Le=1

Table 1 Nusselt number versus buoyancy parameter when Le=1 and $\epsilon_2=0.5$

	$\mathrm{Nu_x}/(\mathrm{Nu_x})_0$		
N	$\epsilon_1=0.1$	$\epsilon_1=0.3$	$\epsilon_1=0.5$
−0.5	0.9375	0.9332	0.9329
0.	0.9821	0.9484	0.9167
0.5	1.0041	0.9541	0.9059
1.0	1.0184	0.9572	0.8973
3.0	1.0507	0.9619	0.8741
5.0	1.0694	0.9635	0.8585

Table 2 Sherwood number versus buoyancy parameter when Le=1 and $\epsilon_1=0.5$

	$\mathrm{Sh_x}/(\mathrm{Sh_x})_0$		
N	$\epsilon_2=0.1$	$\epsilon_2=0.3$	$\epsilon_2=0.5$
−0.5	1.0888	1.0811	0.9329
0.	1.0469	0.9818	0.9167
0.5	1.0290	0.9671	0.9059
1.0	1.0184	0.9572	0.8973
3.0	0.9978	0.9342	0.8741
5.0	0.9878	0.9205	0.8585

Table 3 Effect of Le on mass transfer coefficient when $N=1$ and $\epsilon_1=0$

	$Sh_x/(Sh_x)_0$		
ϵ_2	Le=1	Le=5	Le=10
0	1.0000	1.0000	1.0000
0.1	1.0333	1.1179	1.2062
0.3	1.1057	1.4618	2.0488
0.5	1.1870	2.1053	6.7694

the thermal stratification parameter while the oscillations are set in when the concentration stratification parameter is increased beyond a limit. This feature can be observed from the Fig. 4.

For large value of Le, $\alpha \gg D$ and thermal diffusion is predominant, the temperature profile decreases to zero without any change of sign in the boundary layer. By increasing the solutal stratification parameter, the value of $\phi(0)$ becomes negative for large values of ϵ_2. Also, the negative values are significant and they creep into the boundary layer. This is clearly seen from Fig. 3. For large Le and fixed ϵ_2, increasing the value of ϵ_1 increased the value of $\phi(0)$ and when $\epsilon_1 \gg \epsilon_2$ the concentration distribution become free from oscillations in the boundary layer. When the buoyancy parameter N is large, both the thermal and concentration fields are normal, and the concentration profile crossed the η axis only at large value of ϵ_2. In opposing buoyancy case, large values of solutal stratification resulted in this type of abnormality in the concentration profile. These results are evident from Fig. 5.

The heat and mass transfer from the plate into the doubly stratified porous medium are expressed in terms of the local Nusselt and Sherwood numbers and are defined as

$$\frac{\mathrm{Nu}_x}{(\mathrm{Nu}_x)_0} = \frac{\theta(0)}{\theta(0,\epsilon_1)}$$

where $\mathrm{Nu}_x = q_w x/(T_w - T_\infty)k$ and

$$\frac{\mathrm{Sh}_x}{(\mathrm{Sh}_x)_0} = \frac{\phi(0)}{\phi(0,\epsilon_2)}$$

where $\mathrm{Sh}_x = q_m x/(C_w - C_\infty)D$ with $(\mathrm{Nu}_x)_0$ and $(\mathrm{Sh}_x)_0$ as the values of Nu_x and Sh_x at $\epsilon_1 = 0$ and $\epsilon_2 = 0$, respectively.

For fixed values of Le and ϵ_2, the Nusselt number and the Sherwood number results are tabulated against the buoyancy ratio parameter. The Nusselt number results are presented for three different values of the thermal stratification parameter ϵ_1 in Table 1. The results show the increase in the non-dimensional coefficient with increasing value of the parameter N. Also, increasing the value of ϵ_1 decreased the heat transfer rate into the medium. From Table 2 it is evident that the mass transfer coefficient is a maximum in the case of opposing buoyancy flow. It is also clear that the increase in the parameter N decreased the mass transfer coefficient. Similarly for fixed value of ϵ_1, increase in ϵ_2 lowered the mass transfer rate into the medium.

For fixed values of N and ϵ_1, the effect of Le is observed to favor the mass transfer into the medium. Increase in the value of Le increased the mass transfer coefficient. In the absence of thermal stratification, it further increased the mass transfer co-efficient with increasing solutal stratification parameter value. These results are tabulated in Table 3.

Acknowledgment

The authors are thankful to the journal reviewers and especially to Professor A. S. Gupta of the Department of Mathematics, IIT-Kharagpur for constructive suggestions on the manuscript.

Nomenclature

C = concentration
C_∞, o = ambient concentration at a reference point
D = molecular diffusivity
f = non-dimensional stream function
g = acceleration due to gravity
K = permeability
Le = α/D, Lewis number
k = thermal conductivity
N = $\beta_C q_m k/\beta_T q_w D$, buoyancy ratio
q_w, q_m = wall heat and mass flux constants
Ra_x = modified Rayleigh number, $K_g \beta_T q_w x^2/\alpha \nu k$
T = temperature
T_∞, o = ambient temperature at a reference point
u, v = velocity components in x and y directions respectively
x, y = Cartesian coordinates

Greek

α = thermal diffusivity constant
β_T, β_C = thermal and solutal expansion coefficients
η = similarity variable
ν = kinematic viscosity
ψ = stream function
θ, ϕ = nondimensionl temperature and concentration, respectively
ϵ_1 = $A/3(k_g \beta_T k^2/\alpha \nu q_w^2)^{1/3}$, constant, thermal stratification parameter
ϵ_2 = $B/3(K_g \beta_T D_{q_w}^3/\alpha \nu k q_m^3)^{1/3}$, constant, solutal stratification parameter

Subscripts

w = evaluated at wall
∞ = evaluated at the outer edge of the boundary layer

References

[1] Ludvigsen, A., Palm, E., and Mc Kibbin, R., 1992, "Convective Momentum and Mass Transport in Porous Sloping Layers," J. Geophys. Res. B, **97**, pp. 12315–12325.
[2] Gilman, A., and Bear, J., 1996, "The Influence of Free Convection on Soil Salinization in Arid Regions," Transp. Porous Media, **23**, pp. 275–301.
[3] Cheng, P., 1978, "Heat Transfer in Geothermal Systems," Adv. Heat Transfer, **14**, pp. 1–105.
[4] Bejan, A., and Khair, K. R., 1985, "Heat and Mass Transfer by Natural Convection in a Porous Medium," Int. J. Heat Mass Transfer, **28**, pp. 909–918.
[5] Lai, F. C., and Kulacki, F. A., 1991, "Coupled Heat and Mass Transfer by Natural Convection From Vertical Surfaces in Porous Media," Int. J. Heat Mass Transfer, **34**, pp. 1189–1194.
[6] Trevisan, O. V., and Bejan, A., 1990, "Combined Heat and Mass Transfer by Natural Convection in a Porous Medium," Adv. Heat Transfer, **28**, pp. 315–352.
[7] Nield, D. A., and Bejan, A., 1999, *Convection in Porous Media*, Springer-Verlag, New York.
[8] Bejan, A., 1984, *Convection Heat Transfer*, John-Wiley & Sons, New-York, Chpt. 10.
[9] Singh, P., and Sharma, K., 1990, "Integral Method for Free Convection in Thermally Stratified Porous Medium," Acta Mech. **83**, pp. 157–163.
[10] Kalpana, T., and Singh, P., 1992, "Natural Convection in a Thermally Stratified Fluid Saturated Porous Medium," Int. J. Eng. Sci., **30**, pp. 1003–1007.
[11] Nakayama, A., and Koyama, H., 1987, "Effect of Thermal Stratification on Free Convection With a Porous Medium," AAIA J. Thermophys. Heat Transfer, **1**, pp. 282–285.
[12] Lai, F. C., Pop, I., and Kulacki, F. A., 1990, "Natural Convection from Isothermal Plates in Thermally Stratified Porous Media," AAIA J. Thermophys. Heat Transfer, **4**, pp. 533–535.
[13] Takhar, H. S., and Pop, I., 1987, "Free Convection From a Vertical Flat Plate to a Thermally Stratified Darcian Fluid," Mechanics Research Communications, **14**, pp. 81–86.

Predicting Inlet Temperature Effects on the Pressure-Drop of Heated Porous Medium Channel Flows Using the M-HDD Model

Arunn Narasimhan
Mem. ASME
Staff Research Engineer, Microlithography Division, FSI International, Allen, TX 75013

José L. Lage
Fellow ASME
e-mail: JLL@engr.smu.edu
Laboratory for Porous Materials Applications, Mechanical Engineering Department, Southern Methodist University, Dallas, TX-75275-0337

A Modified Hazen-Dupuit-Darcy (M-HDD) model, incorporating nonlinear temperature-dependent viscosity effects, has been proposed recently for predicting the global pressure-drop of nonisothermal flows across a heated (or cooled) porous medium channel. Numerical simulations, mimicking the flow of a liquid with nonlinear temperature-dependent viscosity, are presented now for establishing the influence of inlet temperature on the pressure-drop and on the predictive capabilities of the M-HDD model. As a result, new generalized correlations for predicting the coefficients of the M-HDD model are derived. The results not only demonstrate the importance of fluid inlet temperature on predicting the global pressure-drop but they also extend the applicability of the M-HDD model. [DOI: 10.1115/1.1667526]

Keywords: Forced Convection, Heat Transfer, Porous Media, Properties, Viscous

1 Introduction

Recent studies on the variable viscosity effects in porous medium flows begin with the work of Ling and Dybbs [1]. They investigated theoretically the influence of temperature-dependent fluid viscosity on the forced convection through a semi-infinite porous medium bounded by an isothermal flat plate. For a similar flat plate configuration, Postelnicu et al. [2] considered the effect of heat generation as well. For non–Darcy flow in the same flat plate porous medium flow configuration, Kumari [3] and [4] provided similarity solutions for mixed convection with variable viscosity, under constant and variable wall heat flux.

While addressing heat transfer effects of variable viscosity porous medium flows, none of the previously cited works studied the impact of variable viscosity on the existing Hazen-Dupuit-Darcy (HDD) model, to predict the pressure-drop across porous medium channels, which was the subject of the pioneering studies in [5] and [6]. This led to the development of the Modified HDD (M-HDD) model, as proposed in [5], incorporating the temperature-dependent viscosity effects in the prediction of global pressure-drop. We shall now proceed, using fresh numerical simulations, to study the influence of changing the inlet temperature on the pressure-drop and on the correction coefficients of the M-HDD model in an effort to extend the applicability of the model.

Contributed by the Heat Transfer Division for publication in the JOURNAL OF HEAT TRANSFER. Manuscript received by the Heat Transfer Division January 31, 2003; revision received September 29, 2003. Associate Editor: V. Prasad.

2 The M-HDD Model and Inlet Temperature Influence

The HDD model (also known as the Darcy-Forchheimer equation),

$$\frac{\Delta P}{L}=\left(\frac{\mu_0}{K_0}\right)U+(\rho C_0)U^2 \tag{1}$$

is rigorously valid for flows of fluids with uniform and constant properties. This model has been generalized as a modified Hazen-Dupuit-Darcy model (M-HDD) in [5] for nonisothermal flows of fluids with temperature-dependent viscosity

$$\frac{\Delta P}{L}=\zeta_\mu\left(\frac{\mu_0}{K_0}\right)U+\zeta_C(\rho C_0)U^2 \tag{2}$$

with the coefficients ζ_μ and ζ_C representing the lumped local effect of temperature dependent viscosity and the effect of viscosity on the fluid velocity profile, respectively, as,

$$\zeta_\mu=\left[1-\left(\frac{Q''}{1+Q''}\right)^{0.325}\right]\left(\frac{1}{1+Q''}\right)^{18.2}\qquad \zeta_C=2+(Q'')^{0.11}-\zeta_\mu^{-0.06} \tag{3}$$

with

$$Q''=\frac{q''}{\left(\frac{k_e}{KC}\right)\mu_0}\left|\frac{d\mu}{dT}\right|_{T_0} \tag{4}$$

Notice in Eqs. (1)–(4), the viscosity and its derivative are evaluated at a reference temperature T_0, and K_0 and C_0 are obtained from Eq. (1) using no-heat experimental results. Therefore, for a heat flux input q'', one can estimate the viscosity variation effects from the M-HDD model, Eq. (2).

The correlations to predict the coefficients of the M-HDD model, Eq. (3), were primarily obtained for poly-alpha-olefin (PAO) in [5] from numerical simulations at a single inlet temperature, i.e., $T_{in}=21°C$. PAO is a very important fluid, used as the base-stock for motor oils and lubricants and the cold-plate coolant of preference in airborne military avionics [7]. The strong temperature-dependent dynamic viscosity of PAO can be modeled [8] as

$$\mu(T)=0.1628T^{-1.0868},\quad 5°C\leqslant T\leqslant 170°C \tag{5}$$

Equation (5), when the values of temperature T are given in °C, predicts the viscosity in Nsm^{-2} within 3% accuracy [10]. Although derived for PAO, Eq. (2) is recommended for fluids having their viscosity behave in a fashion similar to Eq. (5), or following the general form $\mu(T)=AT^{-B}$, where A and B are two constants.

Transport equations and their respective boundary conditions, used to model the momentum and energy transport through a parallel plate porous medium channel with surfaces heated uniformly, and all of the simulation details (e.g., channel dimensions, thermophysical properties, mesh geometry, grid independence tests and convergence criteria used) remain identical with that detailed in [5], [9], and [10].

3 Pressure-Drop Versus Fluid Speed Results

Figures 1 through 3 present results of global pressure-drop versus fluid speed for 7, 21, and 32°C PAO inlet temperature, respectively, and several heat fluxes. The top curve in each of the figures represents the no-heating pressure-drop results. Obviously, the no-heating pressure-drop results could be predicted using the global HDD model, Eq. (1), with the viscosity evaluated at the appropriate inlet temperature ($\mu_0=\mu_{in}=\mu(T_{in})$). The bottom curve in each of the figures is the inviscid pressure-drop result that could be predicted as well by

$$\frac{\Delta P}{L}=\rho C_0 U^2 \tag{6}$$

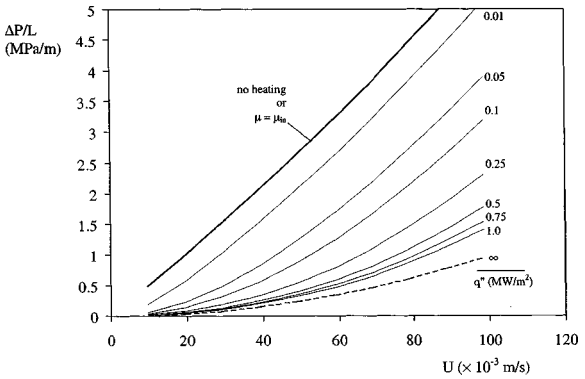

Fig. 1 Longitudinal pressure-drop versus fluid speed for several heat fluxes at $T_{in}=7°C$

the inviscid form-drag limit equation. As the density variation of PAO with temperature is very small (less than one-percent, [7]), obviously this limit can be considered invariant for any inlet temperature.

Proceeding from Figs. 1 to 3, it is apparent that for the same heat flux variation the reduction in the global pressure-drop becomes less evident. If we recall that the inviscid drag limit is the same no matter the inlet temperature (i.e., the location of the dashed line in Figs. 1, 2, and 3), we can reason that a hotter fluid (increased inlet temperature, thereby, smaller inlet viscosity) already has a weaker viscous drag term to begin with. Therefore, the pressure-drop of a stream of fluid with higher inlet temperature suffers less the heating effect on the viscosity. Moreover, heating a cold fluid stream shows a more pronounced effect on the viscous

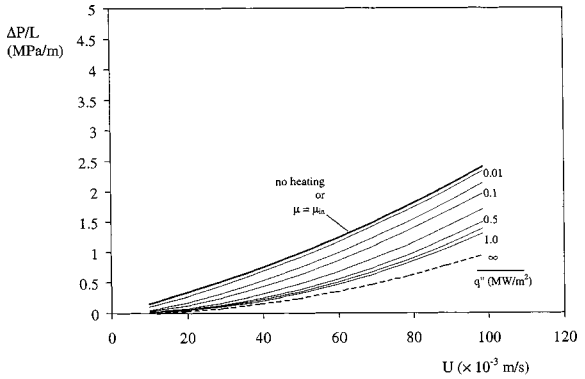

Fig. 2 Longitudinal pressure-drop versus fluid speed for several heat fluxes at $T_{in}=21°C$

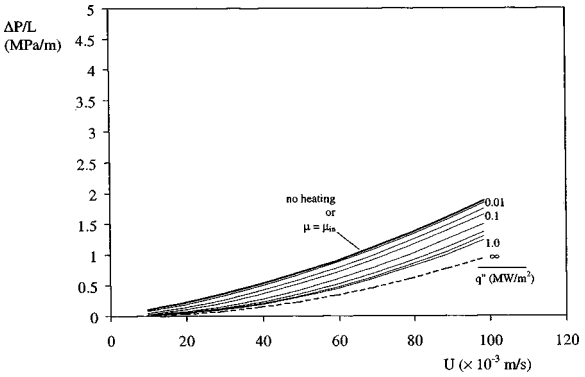

Fig. 3 Longitudinal pressure-drop versus fluid speed for several heat fluxes at $T_{in}=32°C$

drag term because the viscosity at lower temperatures is more sensitive to heating than at a higher temperature (see viscosity Eq. (5)).

Another subtle reason is that reducing the viscosity by increasing the inlet temperature reduces the magnitude of the global viscous drag term (second term in Eq. (2)) directly, even if the channel remains isothermal. However, the global form drag (third term in Eq. (2)) is not affected for isothermal flows, even if the inlet temperature is altered. It is affected only when the flow becomes non-isothermal (here, because of heating) whereby, because of the viscosity variation, the velocity profiles are altered, leading to non-slug flow profiles. Furthermore, the hotter the flow becomes, the extent to which the velocity profiles are altered from their original slug flow like profiles is greatly reduced, leading to a reduction in global form drag variation. This is explained in detail in [9].

4 Inlet Temperature Influence on the Correction Coefficients

The behavior of the correction coefficients (ζ_μ and ζ_C) can be predicted for several heat fluxes by using the M-HDD model, Eq. (2) to curve-fit the numerical pressure-drop results.

An average deviation defined as

$$\sigma=\frac{\left[\frac{1}{N}\Sigma_1^N(\Delta P/L_\zeta-\Delta P/L_{\text{num}})^2\right]^{1/2}}{\frac{1}{N}\Sigma_1^N(\Delta P/L_{\text{num}})} \tag{7}$$

is used for analyzing the goodness of the fit. In Eq. (7), N is the sample size of the pressure-drop versus fluid speed data for each of the heat flux values, for one inlet temperature. Further, $\Delta P/L_\zeta$ is the pressure-drop results predicted through the curve-fit procedure (using Eq. (2)) while $\Delta P/L_{\text{num}}$ is the pressure-drop results (data points) from the numerical simulations.

Notice in the function defined in Eq. (7), the numerical pressure-drop results are taken as the fixed ''reference'' values as the results predicted by the curve-fitting procedure is compared to them. The curve-fitting procedure is further detailed in [7].

From the curve fitting results, a common curve-fitting function, one each for the two ζs of the M-HDD model, Eq. (2), predicting the inlet temperature influence, is proposed. The results of the curve-fit are shown in Fig. 4.

The form of the original, empirical, ζ curve-fit function (Eqs. (3) and (4)) proposed in [5] and the one to be proposed here are conceived with the standard technique discussed in detail in [11] and [12]. Notice from Eqs. (3) and (4), that, $\zeta_\mu=\zeta_C=1$ for $q''=0$ (i.e., for no heating, for any inlet temperature) and $\zeta_\mu\to 0$ and

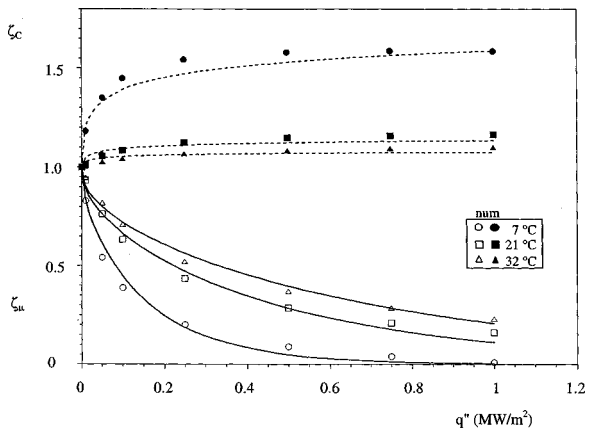

Fig. 4 ζ_μ and ζ_C versus q'', and their curve-fit for several inlet temperatures

$\zeta_C \to 1$ for $q'' \to \infty$ (again, for any/all inlet temperature), for any general porous flow configuration where predictions from the M-HDD model, Eq. (2), is sought. We also invoke the reference temperature method of accounting for viscosity variation effect—a standard practice in forced convection literature [13], to modify suitably the existing constant-viscosity correlation for the heat transfer coefficient (Nu).

Based on the above discussions, the following correlation is proposed for predicting the correction factors of the M-HDD model, Eq. (2),

$$\zeta_\mu = \left[1 - \left(\left(\frac{\mu(T_{in})}{\mu(T_r)}\right)^{0.15} \frac{Q''}{1+Q''}\right)^{0.28}\right]\left(\frac{1}{1+Q''}\right)^{45};$$

$$\zeta_C = 2 + \left(\left(\frac{\mu(T_{in})}{\mu(T_r)}\right)^{5} Q''\right)^{0.2} - (\zeta_\mu)^{-0.01} \tag{8}$$

with the non-dimensional group Q'', given as before, by Eq. (4) and T_r being a suitable reference temperature based on the particular fluid.

In the present case, where the fluid is PAO, the reference temperature $T_r = 7°C$ is chosen close to the lower bound of Eq. (5), the equation predicting the functional dependence of viscosity on temperature. Notice, by doing this, when $T_r = T_{in} = 7°C$, the group $\mu(T_{in})/\mu(T_r)$ in Eq. (8) is equal to unity.

Equation (7) is again used to analyze the goodness of the fit (done using Eq. (8)) in Fig. 4, by suitably modifying the variables. The error range of ζ_μ curve fits (i.e., the deviation of the curve-fit value of ζ_μ from that of its corresponding data point in Fig. 4, which were in turn got by using Eq. (2) to curve-fit the numerical pressure-drop data, as explained in the earlier section) for $T_{in} = 7°C$, is 40 to 60% for the last three heat flux values. Although this seems alarming, the actual ζ_μ values for these three heat fluxes is already less than 0.05, ensuring a very weak global viscous drag regime anyway (see [7] for a more elaborated discussion). The curve fitting function, Eq. (8), predicts the rest of the ζ_μ and ζ_C data with accuracy within six percent, which is considered good.

The usefulness of the empirical relations, Eq. (8), is apparent as most of the practical engineering applications involving coolants like PAO, water and ethyl alcohol, operate within the heat flux range that keeps the temperature of the convecting coolant flow within the range of application of Eq. (5). In other words, this is the range within which an engineer is interested in the M-HDD model's predictions for the thermo-hydraulic performance.

5 Summary and Conclusion

Using fresh numerical simulations, the influence of inlet temperature on the M-HDD model has been studied. For increasing heat flux, the degree of reduction in the global pressure-drop decreases with increase in inlet temperature, because of the nonlinear temperature dependence of the viscosity, Eq. (5). New empirical correlations, Eq. (8), capturing the inlet temperature influence on the correction factors of the M-HDD model, Eq. (2), have been proposed. Although obtained primarily for PAO, these correlations are recommended for fluids having their viscosity behave in a similar fashion to Eq. (5). Within this range, the correlations that are proposed in Eq. (8) are extremely relevant and practical.

Nomenclature

C = form coefficient, m^{-1}
K = permeability, m^2
L = channel length, heated section, m
U = global (cross-section averaged) longitudinal velocity, $m\,s^{-1}$
σ = deviation
ζ = coefficients

Subscripts

C = form
e = effective
f = fluid
in = inlet
r = reference
s = solid
0 = isothermal condition
μ = viscous

References

[1] Ling, J. X., and Dybbs, A., 1992, "The Effect of Variable Viscosity on Forced Convection Over a Flat Plate Submersed in a Porous Medium," ASME J. Heat Transfer, **114**, pp. 1063–1065.

[2] Postelnicu, A., Grosan, T., and Pop, I., 2001, "The Effect of Variable Viscosity on Forced Convection Flow Past a Horizontal Flat Plate in a Porous Medium With Internal Heat Generation," Mechanics Research Communications, **28**, pp. 331–337.

[3] Kumari, M., 2001, "Effect of Variable Viscosity on Non-Darcy Free or Mixed Convection Flow on a Horizontal Surface in Saturated Porous Medium," Int. J. Heat Mass Transfer, **28**(5), pp. 723–732.

[4] Kumari, M., 2001, "Variable Viscosity Effects on Free and Mixed Convection Boundary-Layer Flow From a Horizontal Surface in a Saturated Porous Medium—Variable Heat Flux," Mechanics Research Communications, **28**(3), pp. 339–348.

[5] Narasimhan, A., and Lage, J. L., 2001, "Modified Hazen-Dupuit-Darcy Model for Forced Convection of a Fluid With Temperature Dependent Viscosity," ASME J. Heat Transfer, **123**, pp. 31–38.

[6] Narasimhan, A., Lage, J. L., Nield, D. A., and Porneala, D. C., 2001, "Experimental Verification of Two New Theories for Predicting the Temperature-Dependent Viscosity Effects on the Forced Convection Through a Porous Media Channel," ASME J. Fluids Eng., **123**, pp. 948–951.

[7] Narasimhan, A., 2002, "Unraveling, Modeling and Validating the Temperature Dependent Viscosity Effects in Flow Through Porous Media," Ph.D. dissertation, Southern Methodist University, Dallas, TX.

[8] Porneala, D. C., 1998, "Experimental Tests of Microporous Enhanced Cold Plates for Cooling High Frequency Microwave Antennas," Ph.D. dissertation, Southern Methodist University, Dallas, TX.

[9] Narasimhan, A., and Lage, J. L., 2001, "Forced Convection of a Fluid With Temperature-Dependent Viscosity Through a Porous Medium Channel," Numer. Heat Transfer, **40**(8), pp. 801–820.

[10] Lage, J. L., Antohe, B. V., and Nield, D. A., 1997, "Two Types of Nonlinear Pressure-Drop Versus Flow-Rate Relation Observed for Saturated Porous Media," ASME J. Fluids Eng., **119**, pp. 700–706.

[11] Churchill, S. W., and Usagi, R., 1972, "A General Expression for the Correlation of Rates of Transfer and Other Phenomena," AIChE J., **18**(6), pp. 1121–1128.

[12] Churchill, S. W., and Ozoe, H., 1973, "Correlations for Laminar Forced Convection With Uniform Heating in Flow Over a Plate and in Developing and Fully Developed Flow in a Tube," ASME J. Heat Transfer, **95**, pp. 78–84.

[13] Kakaç, S., 1987, "The Effect of Temperature-Dependent Fluid Properties on Convective Heat Transfer," in *Handbook of Single-Phase Convective Heat Transfer*, Kakaç et al., Eds., John Wiley and Sons, New York, Chpt. 18.